Biophysical Journal Volume 108 May 2015 2312–2321

Article

Force-Sensitive Autoinhibition of the von Willebrand Factor Is Mediated by Interdomain Interactions

Camilo Aponte-Santamaría,[1] Volker Huck,[2] Sandra Posch,[3] Agnieszka K. Bronowska,[1] Sandra Grässle,[2] Maria A. Brehm,[4] Tobias Obser,[4] Reinhard Schneppenheim,[4] Peter Hinterdorfer,[3] Stefan W. Schneider,[2] Carsten Baldauf,[5,*] and Frauke Gräter[1,*]

[1]Molecular Biomechanics Group, Heidelberg Institute for Theoretical Studies, Heidelberg, Germany; [2]Experimental Dermatology, Medical Faculty Mannheim, Heidelberg University, Mannheim, Germany; [3]Department of Applied Experimental Biophysics, Institute of Biophysics, Johannes Kepler University, Linz, Austria; [4]Department of Pediatric Hematology and Oncology, University Medical Center Hamburg-Eppendorf, Hamburg, Germany; and [5]Theory Department, Fritz-Haber-Institut der Max-Planck-Gesellschaft, Berlin, Germany

ABSTRACT Von Willebrand factor (VWF) plays a central role in hemostasis. Triggered by shear-stress, it adheres to platelets at sites of vascular injury. Inactivation of VWF has been associated to the shielding of its adhesion sites and proteolytic cleavage. However, the molecular nature of this shielding and its coupling to cleavage under shear-forces in flowing blood remain unknown. In this study, we describe, to our knowledge, a new force-sensory mechanism for VWF-platelet binding, which addresses these questions, based on a combination of molecular dynamics (MD) simulations, atomic force microscopy (AFM), and microfluidic experiments. Our MD simulations demonstrate that the VWF A2 domain targets a specific region at the VWF A1 domain, corresponding to the binding site of the platelet glycoprotein Ibα (GPIbα) receptor, thereby causing its blockage. This implies autoinhibition of the VWF for the binding of platelets mediated by the A1-A2 protein-protein interaction. During force-probe MD simulations, a stretching force dissociated the A1A2 complex, thereby unblocking the GPIbα binding site. Dissociation was found to be coupled to the unfolding of the A2 domain, with dissociation predominantly occurring before exposure of the cleavage site in A2, an observation that is supported by our AFM experiments. This suggests that the A2 domain prevents platelet binding in a force-dependent manner, ensuring that VWF initiates hemostasis before inactivation by proteolytic cleavage. Microfluidic experiments with an A2-deletion VWF mutant resulted in increased platelet binding, corroborating the key autoinhibitory role of the A2 domain within VWF multimers. Overall, autoinhibition of VWF mediated by force-dependent interdomain interactions offers the molecular basis for the shear-sensitive growth of VWF-platelet aggregates, and might be similarly involved in shear-induced VWF self-aggregation and other force-sensing functions in hemostasis.

INTRODUCTION

Von Willebrand Factor (VWF) is a giant extracellular protein playing a key adhesive role in blood clotting. Activated by shear-stress, this protein cross-links the extracellular matrix of the endothelium with blood platelets, at sites of vascular injury (1,2). It efficiently participates in the shear-induced reversible formation of biopolymer-colloid aggregates (3), and its malfunction leads to pathological bleeding and thromboembolic disorders (1).

Functional VWF is a linear multimer of tens of covalently linked monomers (4), extending up to 15 μm (5). Each monomer, with a length of 60 to 80 nm (2,6), comprises 2050 amino acids in domains of few nm in size (7). The large size in the μm range enables VWF multimers to sense changes in the shear flow of blood and to translate them into a mechanical stretching force along the protein chain (5,8,9). Shear-forces, by inducing a tumbling motion alternating between globular and extended states, facilitate the adhesion of VWF to the extracellular matrix (5,10) and to flowing platelets (3).

The VWF A1 and A2 domains are critical for the activation of VWF to bind platelets and for its deactivation by size control. These two domains are adjacent to each other and connected by a linker of $\sim$ 30 amino acids (Fig. 1 *A*). X-ray crystallography revealed that both domains adopt a stable Rossmann α/β-fold (11,12), stabilized by calcium in the case of A2 (13,14). Platelets bind through the glycoprotein Ibα (GPIbα) to a region of the A1 domain (15,16), in a shear-dependent manner (17–21). For size control, the A2 domain is cleaved by the metalloprotease ADAMTS13 (22), after exposure of the Y1605-M1606 (YM) cleavage site, because of shear-induced domain unfolding (23–27).

Under equilibrium or under low shear-stress conditions, VWF is incapable of binding platelets. This inactivation has been associated with a shielding of the GPIbα binding site of A1. Recent experiments revealed that, in addition to the D'D3 domains (28) and the linker connecting them to the A1 domain (29), isolated A2 domains modulate glycoprotein Ib (and thereby platelet) binding (30,31). However, electron microscopy (EM) images established the separation between these two domains, within the same VWF molecule, from 4.4 to 11 nm (6), challenging the inhibitory

Submitted October 10, 2014, and accepted for publication March 18, 2015.

*Correspondence: frauke.graeter@h-its.org or baldauf@fhi-berlin.mpg.de

Editor: Nathan Baker

0006-3495/15/05/2312/10 $2.00

http://dx.doi.org/10.1016/j.bpj.2015.03.041

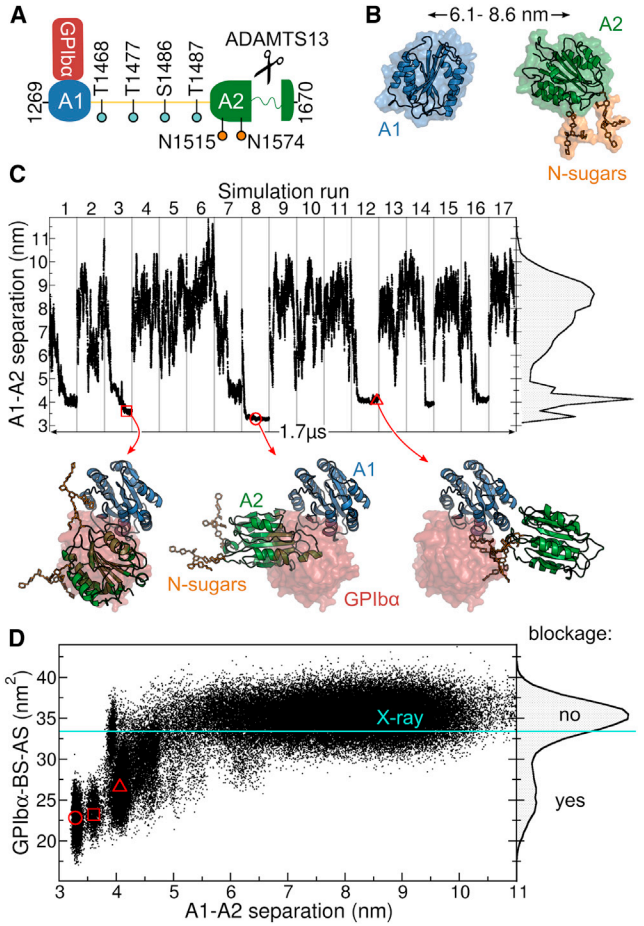

FIGURE 1 Blockage of the GPIbα binding site in the VWF revealed by MD simulations of the VWF A1 and A2 domains. (*A*) Scheme illustrating the human VWF-A1A2 fragment (residues 1269 to 1670). The A1 and A2 domains are connected by a 30 residue linker (*yellow*). GPIbα anchors platelets to VWF by binding to the A1 domain. VWF size is controlled by cleavage of the unfolded A2 domain by ADAMTS13. O-linked (*cyan*) and N-linked sugars (*N-sugars, orange*) are found within the fragment. (*B*) One of the multiple starting conformation used in the MD simulations (*protein as cartoon and surface and sugars as sticks*). The domain-domain center of mass (A1-A2) separation is indicated with the black arrow. (*C*) A1-A2 separation along the concatenated MD simulation time. Gray lines separate individual MD runs. The right plot shows the normalized histogram of the A1-A2 separation. Conformations at the bottom show examples with the two domains in contact (*cartoon*) contrasted to the region occupied by GPIbα when it binds to A1 (*red surface*), taken at the instants marked with the red symbols. (*D*) GPIbα binding site accessible surface (GPIbα-BS-AS) as a function of the A1-A2 separation (*main panel*) and its normalized histogram (*right plot*), recovered from MD simulations. Reduced GPIbα-BS-AS values indicate blockage of the GPIbα binding site. The GPIbα-BS-AS derived from the VWF A1-GPIbα complex x-ray structure (16) is depicted by the cyan line. The red symbols correspond to the conformations shown in (*C*). To see this figure in color, go online.

role of A2 on A1. Hence, little is known on how these two domains interact with each other, causing inhibition, and how sensitive this interaction is to shear-forces in flowing blood. It also remains unclear how VWF activation, through the release of the GPIbα binding site, and VWF deactivation, through unfolding of the A2 domain, are mechanically regulated to balance the propagation and attenuation of hemostasis. We addressed these questions by performing molecular dynamics (MD) simulations of the VWF A1 and A2 domains, under equilibrium and force-probe conditions, together with molecular docking calculations, atomic force microscopy (AFM) binding measurements, and microfluidic experiments. To our knowledge, our results suggest a novel mechanism for shear-dependent primary hemostasis, involving a force-sensitive autoinhibition state, in which platelets are incapable to bind to VWF because of direct (intra- or intermolecular) A1-A2 interactions precluding the A1-GPIbα interaction.

MATERIALS AND METHODS

Equilibrium MD simulations

In the first simulation system, the A1 and A2 domains of the VWF were not covalently connected by their interdomain linker. They were either initially separated by distances from 6.1 to 8.6 nm to monitor association or already bound in conformations blocking the GPIbα binding site (obtained by docking, see below) for refinement. The second simulation system corresponded to the VWF-A1A2 fragment consisting of the A1 and A2 domains connected by a 30 amino acid linker, with an initial interdomain separation of 7.9 nm based on EM estimates (6). The most predominantly found sugars in the VWF glycome (32,33) were attached to the protein (Fig. 1 *A* and Fig. S1 in the Supporting Material). Simulations were carried out with the GROMACS package (4.5 version) (34–36). Sixteen or 17 runs, considering multiple interdomain initial orientations, were performed for each condition ($\geq$ 82 ns per run) yielding a concatenated simulated time of 4.86 μs. The GPIbα binding site accessible surface (GPIbα-BS-AS) was computed by monitoring the amount of exposed surface of the GPIbα binding site in the A1 domain. A principal component analysis (PCA), consisting in the calculation and diagonalization of the covariance matrix of the atomic coordinates (37), was employed to monitor the interdomain orientations (Fig. 2). The solvent accessible hydrophobic surface (SAHS) reduction was estimated as [SAHS(A1A2) − SAHS(A1) − SAHS(A2)]/[SAHS(A1) + SAHS(A2), computing separately the surface for the complex (A1A2) and for the domains A1 and A2.

Force-probe MD simulations

The A1 and A2 domains of the VWF were subjected to external harmonic forces on the N-terminus of the A1 domain and on the C terminus of the A2 domain (Fig. 3 *A*). Harmonic springs (with elastic constants of 500 kJmol^{-1}nm^{-2}) were attached to these termini and moved away from each other at a speed of 0.2 m/s. These simulations were started from 17 different starting conformations: one was extracted from an equilibrium MD run showing spontaneous binding (run number eight in Fig. 1 *C*) and the remaining 16 corresponded to representative conformations of the equilibrium simulations of the VWF-A1A2 complex (one conformation taken from each run presented in Fig. 2 *A*). Hence, starting conformations with high but also moderate stability were considered. The two monomers were not connected, first, to resemble dissociation of the A1-A2 complex either within or across VWF monomers (preventing from possible artifacts by the inclusion of the flexible linker for which the structure is unknown), and second, to have a direct comparison with our AFM experiments (also carried out with nonconnected domains, see below). Dissociation was assigned to the moment when the interdomain number of contacts was zero. Detachment of the A2-β5 strand from the core of the A2 domain

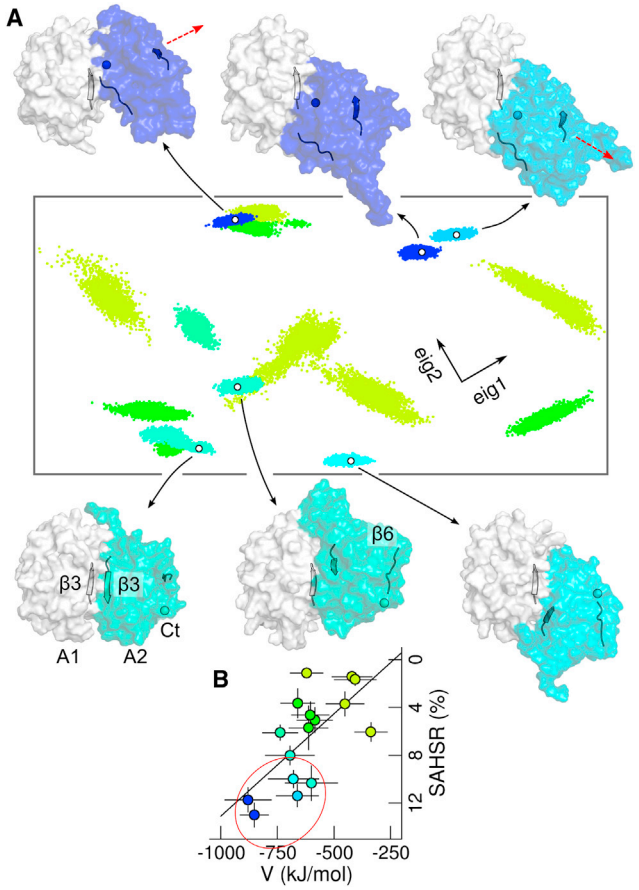

FIGURE 2 Orientational preferences of the VWF-A1A2 complex in the blocked state. (*A*) Principal component analysis (PCA) of the structures of the not-covalently linked VWF-A1A2 complex, with the GPIbα binding site blocked, predicted by molecular docking, yielded two main collective vectors (eig1 and eig2). MD trajectories (the last 50 ns) starting from these structures were projected onto the two-dimensional (2D) space created by these two vectors (projections in arbitrary units). Each dot, representing a simulation snapshot, reflects an adopted interdomain orientation. Each run is colored according to its interdomain potential interaction energy, V, and average solvent accessible hydrophobic surface reduction, SAHSR (see *B*). Representative orientations of runs with both high V and SAHSR (*enclosed by the red circle in B*) are displayed (*A1 domain*, *white*; *A2 domain*, *color*; *β3 strands*, *cartoon*; *A2 β6 strand*, *ribbon*, *and A2 C terminus*, *sphere*). The red arrows illustrate the change in orientation of A2 on horizontal changes in the 2D-PCA space. (*B*) SAHSR as a function of V (time-average ± standard deviation from the last 50 ns of each run). Colors indicate the projection along a linear fit (*black line*), with both V and SAHSR ranging from small (*light green*) to large (*blue*) values. To see this figure in color, go online.

was monitored by measuring the distance between V1625-P1627 (at β5) and V1604-Y1605 (at β4).

Molecular docking

To augment the MD-generated conformational ensemble of the VWF-A1A2 complex, with a blocked GPIbα binding site, we used molecular docking. Two independent docking approaches, either using Patchdock (38) with further refinement with Firedock (39) or using RosettaDock (40) were considered. Starting conformations of the MD simulations with

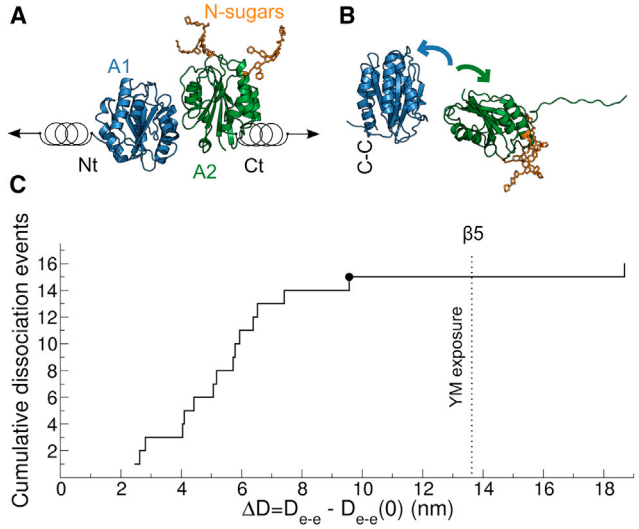

FIGURE 3 Force response of the VWF-A1A2 complex from force-probe MD simulations. (*A*) The N-terminus (Nt) of the A1 domain and the C terminus (Ct) of the A2 domain were pulled away from each other by harmonic springs. The domains were initially in contact but not connected by a linker (*domains in cartoon and N-linked sugars in stick representation*). (*B*) Snapshot illustrating a typical dissociation event of the VWF-A1A2 complex induced by the applied force (same representation as in *A*). Slight unfolding of the C-terminal part of the A2 domain was observed. The disulfide bond Cys1272-Cys1458 (C-C) prevented the A1 domain from unfolding. (*C*) Cumulative dissociation events (from 17 runs) as a function of the distance D_{e-e} between the pulled N- and C termini at the moment of dissociation. Here, $\Delta D = D_{e-e} - D_{e-e}(0)$, subtracting the initial distance $D_{e-e}(0)$, is shown. The Y1605-M1606 (YM) ADAMTS13 cleavage site was exposed after separation of the A2 C-terminal β5 strand from the core of the protein (*event indicated by the dotted line*). The black circle corresponds to the dissociation event illustrated in (*B*). To see this figure in color, go online.

the domains in contact were generated by Patchdock and Firedock (see selection criterion in Fig. S3).

Cloning, expression, and purification of VWF constructs

The cDNAs coding for either the full-length human VWF, or the A1, A2, and A3 domain, the latter three with 6x His-tag, were cloned into the mammalian expression vector pcDNA3 (41). ΔA1-VWF and ΔA2-VWF mutants were obtained by deleting either the A1 or the A2 domain from the full-length cDNA, by site-directed mutagenesis, employing the QuickChange kit (Stratagene, La Jolla, CA). All primers are available on request. Recombinant expression of VWF constructs in HEK293-EBNA cells was performed as described (42) and the His-tagged VWF domain constructs were purified employing the His-Pur Ni-NTA Resin (Thermo Scientific, Waltham, MA).

AFM

Force distance cycles (FDC) were acquired by approaching and retracting the VWF A1 domain (C-terminally linked to the AFM cantilever by maleimide-polyethylene glycol (PEG)-NHS -mPN- molecules) to VWF A2 domains (C-terminally immobilized on a mica surface by mPN linkers). The disulfide bond Cys1272-Cys1458, connecting the N- and C terminus of the A1 domain, ensured a high similarity of the pulling geometry in

the force-probe MD simulations (pulling the N-terminus) and the AFM experiments (pulling the C terminus). Binding events were discerned from nonspecific adhesion by how much they differed in the approach and retraction force signals. To have an unbiased choice of binding events, FDC displaying a characteristic worm-like-chain-type force signal, as well as FDC not showing such behavior, were included for further analysis. To validate specific binding, control experiments were carried out either in the presence of 0.1 mg/ml soluble A2 domains or by replacing either the A1 or the A2 domain by VWF A3 domains. The latter case constitutes a critical control experiment, because A3 is a protein domain that is in the vicinity of A1 and A2 in physiological conditions, and also has the Rossmann topology. For each system, four cantilever tips were utilized. At least 1000 FDC were recorded for each of the tips at a pulling speed of 600 nm/s.

The elongation L corresponded to the extension of the A1 and A2 domains, together with the ones of the mPN linkers and 3-aminopropyltriethoxy silane (APTES) coating molecules. It was measured, during a binding event, as the distance in which the attraction and retraction force-distance curves differed minus the cantilever deflection CD (Fig. 4 *A*). In practice, L + CD was measured by fitting a second-order polynomial to the force curves, followed by the determination of the point in the retraction curve where the force abruptly returned back to zero. The cantilever deflection CD was determined as the applied stretching force F (extracted at the moment of rupture during the FDC) divided by the actual spring constant of the cantilever (30 pNnm^{-1}). The expectation value of L (EV) was estimated as EV = $\sum_i P_i L_i$, with P_i the measured probability to have an elongation of L_i, summing over all the measured L_i values. To account for the size of the A1 domain and the mPN linkers, $l_{A1} + 2l_l$ was subtracted to each measured elongation L. The size of the A1 domain (l_{A1}) was estimated as 2 × its radius of gyration (1.6 nm, derived from MD simulations of the isolated A1 domain (43)). A worm-like-chain model was employed to compute the extension l_l of the mPN linkers as a function of the force F. It reads as follows:

$$\frac{FP}{k_BT} = \frac{1}{4}\left(1 - \frac{l_l}{lc}\right)^{-2} - \frac{1}{4} + \frac{l_l}{lc},$$

where P is the persistence length (0.38 nm (44)), l_c is the mPN linker contour length (8.9 nm, considering 27 PEG units and 0.33 nm per unit), k_B is the Boltzmann constant, and T is the temperature. The cumulative distributions of both the original elongation L and its theoretical reduction (accounting for the size of A1 and linkers) were shown.

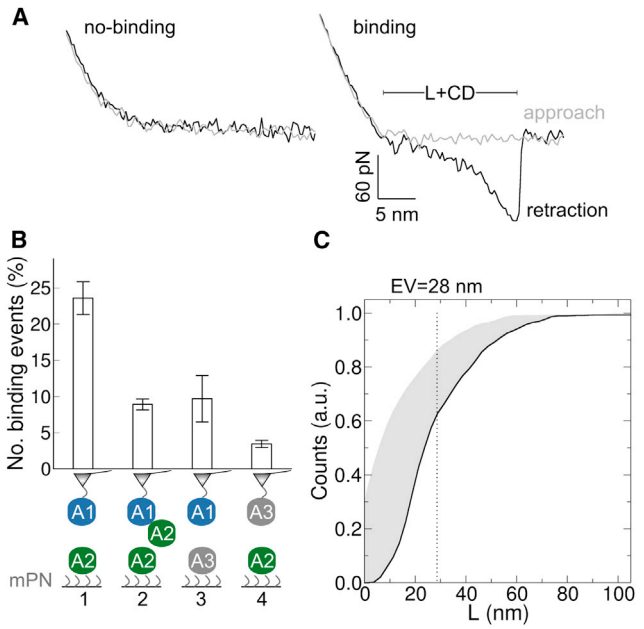

FIGURE 4 Force response of the VWF-A1A2 complex from AFM. (*A*) Typical approach-retraction force-distance profiles associated to no-binding and binding events. The elongation L, of the A1 and A2 domains, together with the mPN linkers and the 3-aminopropyltriethoxy silane coating molecules, summed to the cantilever deflection (CD) was determined by the difference between approach and retraction curves. (*B*) (*1*) Number of binding events between VWF A1 and A2 domains. A1 was connected to the tip of the AFM cantilever (*triangle*) using malemide-PEG-NHS (mPN) linkers. It was approached to and retracted from the surface carrying mPN-linked A2 domains. Force-distance cycles presented in (*A*) correspond to this situation. (*2–4*) Number of binding events measured in control AFM experiments, in which the A1 domain was blocked by soluble A2 domains (*2*), or either the A2 domains on the surface (*3*) or the A1 domain connected to the cantilever (*4*) were replaced by VWF A3 domain. (*C*) Cumulative distribution of L (*black line*) and its correction by subtracting the size of A1 and the mPN linkers (*gray area*). Dotted line indicates the expectation value (EV) of L. To see this figure in color, go online.

Microfluidic experiments

For distinct shear rate application, air-pressure driven microfluidic channels were coated with recombinant wild-type VWF, ΔA2-VWF, or ΔA1-VWF. For the functional characterization, the coated microfluidic channels were mounted onto an inverted fluorescence microscope and perfused, as previously published (45), with wild-type VWF, VWF with the A2 domain deleted, or VWF with the A1 domain deleted. Live cell fluorescence images were taken and analyzed at shear rates in the range of 500 s^{-1} to 4000 s^{-1}. To track the motion of VWF-platelet fibers and aggregates, an image composition of 20 sequential frames (taken at a frequency of two frames/s) was implemented. Increasing number of frames was considered for the composition (from one to all 20 frames), subtracting identical pixels among frames. Dynamical monitoring allowed the exact determination of the critical shear rate for VWF-platelet fiber and aggregate formation.

See further details of the simulations and the experimental procedures in the Supporting Material.

RESULTS

Blockage of the VWF GPIbα binding site in A1 by A2

We first investigated whether the VWF A2 domain spontaneously binds to the A1 domain. To this end, we carried out 17 independent 100 ns equilibrium MD simulations, starting with these two domains separated by distances (between their center of masses) from 6.1 to 8.6 nm and adopting different orientations with respect to each other (Fig. 1 *B*). The linker connecting the two domains was not considered (in the following, this situation will be referred as not connected domains). The two domains spontaneously came into contact and remained stably bound in seven out of 17 simulation runs, as reflected by drops in their separation to values smaller than 5 nm (Fig. 1 *C*).

We next analyzed if the GPIbα binding site in the A1 domain was blocked upon binding of the A2 domain. We quantified the amount of blockage by computing the GPIbα binding site accessible surface (GPIbα-BS-AS) (Fig. 1 *D*). The GPIbα-BS-AS histogram recovered from our simulations revealed a major peak close to the value estimated

from the x-ray structure of the VWF A1-GPIbα complex (16) (33.4 nm^2), indicating no blockage. In addition, the histogram contained a tail extending to values smaller than 20 nm^2, reflecting substantial blockage (of more than 40% of the x-ray GPIbα-BS-AS). Remarkably, blockage was found correlated with the separation between domains, with the GPIbα binding site fully accessible (large GPIbα-BS-AS) only for large interdomain separations, whereas completely blocked (small GPIbα-BS-AS) when the A2 domain approached the A1 domain. Thus, from our simulations, A2 binding to A1 implies blockage of the VWF-GPIbα interaction site.

We also tested the blockage of the GPIbα binding site within a VWF-A1A2 fragment, with the A1 and A2 domains connected by the linker. We simulated the dynamics of such fragment, in 16 independent MD runs of 82 to 100 ns, with initial interdomain separations (∼ 7.9 nm) and linker extensions (∼ 6.0 nm) taken from EM estimates (6) (Fig. S2 *A*). The fragment populated the lower range of separations measured in the EM experiments (6) (Fig. S2 *B*). Again, the MD-generated conformations included several instances of direct A1-A2 interactions (Fig. S2 *B*). The presence and involvement of the O-linked glycosylated linker now alleviated the strong correlation between A1-A2 binding and blockage of the GPIbα binding site as observed for not connected domains (Fig. S2 *C*).

Orientational preferences in the blocked state

Our simulations raised the question on the most-favorable conformation of the two domains with GPIbα binding blocked. We addressed this by performing molecular docking followed by MD refinement. We generated a set of conformations by docking the A2 domain to the A1 domain. From this set, we selected representative conformations with both the GPIbα binding site blocked and high docking score as starting positions of 16 MD simulations of 100 ns each (see Fig. S3 and the Supporting Material for the selection criterion). Similar conformations presenting blockage were predicted by two independent docking approaches (Fig. S4). Furthermore, an enrichment of blocked conformations over random conformations was observed, because of their large interdomain shape complementarity and favorable protein-protein interactions, thus justifying our selection criterion of only blocked and high-docking-score structures (Fig. S5 and the Supporting Material).

During the simulations the domains remained bound causing blockage, while maintaining their internal structure almost intact (backbone root-mean-square deviation to the initial structure below 1.5 Å for A1 and 2.3 Å for A2), but accommodating with respect to each other in multiple orientations. To capture the extent of stable blocking interdomain orientations we carried out a PCA of the conformations predicted by docking (yielding two main collective eigenvectors covering 68% of the possible interdomain orientations), followed by projections of the MD trajectories onto the two-dimensional (2D) space generated by these two vectors (Fig. 2 *A*). Furthermore, we narrowed the orientations to those with high interdomain potential energy, V, and substantial solvent accessible hydrophobic surface reduction (SAHSR) (Fig. 2 *B*). Remarkably, in all orientations with large V and SAHSR contributions, the A2 domain was found directly obstructing the A1-domain β3 strand (the one connecting with GPIbα (15,16)) and displaying only small orientational deviations (small point clouds in the 2D-PCA projections), indicating high structural integrity. Within this preferred set of VWF-A1A2 complexes, the A2 domain oriented in two main modes: either with its C terminus in proximity to the A1 domain or—on ~180° relative rotation—with its β3 strand in proximity, almost forming a stable interdomain β-sheet in the latter case (compare top with bottom projections and snapshots in Fig. 2 *A*). The residues Arg1668 and Asp1587, both in A2, were found to strongly interact with A1: Arg1668, when the C terminus was in proximity to A1, and Asp1587, when the β3-strand was in vicinity. Destabilizing mutations Arg1668Asp and Asp1587Lys are thus potential candidates to detect the most favored conformation of the complex among the two observed orientational modes. In addition, replacement of Val1548 located directly at the β3 strand of A2, for instance by a bulky polar residue such as serine or asparagine, would further distort the orientational mode that features a quasi interdomain β-sheet.

We validated the observed orientational preferences by comparing this with our previous set of simulations (Fig. S6). The docking-MD refined region was also sampled during the MD simulations starting from separated domains, with the A2 domain located directly in front of the β3 strand of the A1 domain. However, the conformational ensemble in the blocked state was further broadened presumably because of the sugars and also the linker between A1 and A2.

VWF-A1A2 complex under force: activation versus cleavage

Induced by shear-forces, the release of the GPIbα binding site in the A1 domain would allow platelet-binding activation, whereas exposure of the YM catalytic site after unfolding of the A2 domain would enable cleavage and degradation. We studied how a stretching force balances these two processes. For this purpose we performed 17 independent force-probe MD simulations, starting from a diverse set of conformations of the two domains, not connected, forming a complex, and with the GPIbα binding site obstructed (Fig. 3 *A*). We pulled the N-terminus of the A1 domain and the C terminus of the A2 domain away from each other, until dissociation of the complex (and thereby unblocking of the GPIbα binding

site) occurred (Fig. 3 *B*). The A2 domain slightly unfolded in its C-terminal part, while the A1 domain remained folded because of its Cys1272-Cys1458 disulfide bond (Fig. 3 *B*).

We quantified the extent of unfolding of the C terminus of the A2 domain by monitoring the increase in the distance between the pulled termini, D_{e-e}, with respect to the initial distance $D_{e-e}(0)$. Exposure of the YM cleavage site, as an initial requirement for ADAMTS13 cleavage, occurred after the detachment of the β5 strand ($D_{e-e} - D_{e-e}(0) \simeq 13.6$ nm). In comparison, dissociation of the fragment, as needed for activation, occurred before YM exposure, in 15 of the 17 runs (88% of the cases) (Fig. 3 *C*).

We next probed the physical interaction between A1 and A2 and the coupling between dissociation and unfolding, as suggested by our simulations, at the single-molecule level by using AFM (Fig. 4). FDC were acquired by approaching the A1 domain (linked to the AFM cantilever) to A2 domains (immobilized on a surface) and retracting it again. A retracting force signal differing from the approaching one, with an abrupt drop to zero at dissociation, was used as an indicator for a binding event (Fig. 4 *A*). It was observed in ~23% of the cycles (*1* in Fig. 4 *B*). In contrast, a substantially reduced number of binding events (less than 10%) was observed in the presence of soluble A2 domains, presumably because of the blocking of the A1 domain at the cantilever (*2* in Fig. 4 *B*). As a control, reduction in the number of binding events was also observed when replacing either the A2 domains at the surface (*3* in Fig. 4 *B*) or the A1 domain at the cantilever (*4* in Fig. 4 *B*) by VWF A3 domains. This implies that binding events are exclusively through A1-A2 interactions, thus confirming the observation from our MD simulations and from previous binding assays (30) that the VWF A1 and A2 domains specifically interact.

To further investigate the coupling between dissociation of the VWF-A1A2 complex and unfolding of the A2 domain, we measured the elongation of the complex (together with linkers and coating molecules) before dissociation by AFM (Fig. 4 *C*). The measured expectation value of the elongation (~28 nm) was substantially lower than the extension of a fully stretched unfolded A2 domain (~80 nm (23–27)). In fact, in all FDC, the elongation remained below those levels of extension. Although the noise in the length distribution is expected to be large because of the tip and surface chemistry, our AFM data speak against full unfolding of A2 before dissociation. Instead, it suggests a small extent of unfolding of A2 before dissociation.

Functional characteristics of VWF with the A2 domain deleted in shear-induced fiber formation

We next examined if the A2 domain inhibits VWF-platelet binding in a shear-dependent manner, by performing microfluidic experiments, in wild-type VWF-coated channels, under replacement of the plasmatic wild-type VWF by recombinant VWF with the A2 domain deleted (ΔA2-VWF), and in a wide shear range. In the presence of wild-type VWF in the perfusion medium, above a critical shear rate of 4000 s^{-1}, large aggregates of VWF and platelets were observed to roll along the surface coated with VWF (Fig. 5, *top right*). At lower shear rates, rolling VWF-platelet aggregates were absent. Here, we only observed either rolling of single platelets along the microfluidic channel (at 500 s^{-1}, Fig. 5, *top left*) or reversibly formed platelet-decorated VWF fibers, which stayed attached to the channel surface (at 2500 s^{-1}, Fig. 5, *top middle*). Instead, in the presence of ΔA2-VWF in the perfusion medium, the critical shear rate for rolling aggregate formation was decreased to 2500 s^{-1}, indicating a gain of function for the VWF by deletion of its A2 domain (Fig. 5, *middle*, and Movie S1). Identical results were obtained using ΔA2-VWF instead of wild-type VWF for coating of the microfluidic channels (data not shown). In a multimer analysis, similar VWF size distributions were observed for the mutants and for the wild-type VWF, just slightly shifted down because of the deletions in the mutant proteins (Fig. S7). Changes in the VWF distribution size are thus discarded as the reason for the gain in function of the ΔA2-VWF mutant. As expected, neither fibers nor VWF-platelet aggregates were formed in the presence of VWF with an A1-domain deletion (Fig. 5, *bottom*). Furthermore, coating with ΔA1-VWF led to a complete absence of both single platelet rolling and the formation of rolling

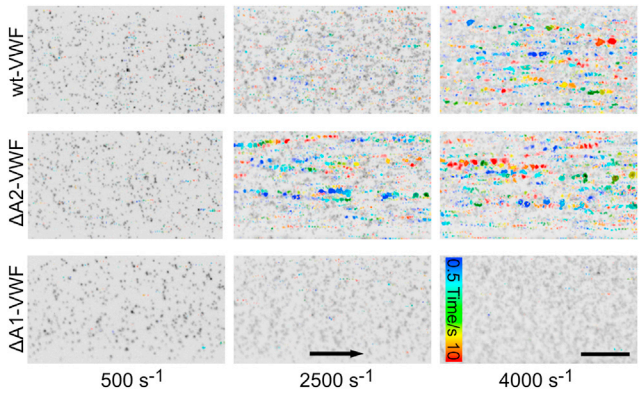

FIGURE 5 Changes in shear-induced fiber and aggregate formation on deletion of the VWF A2 domain. Live-cell fluorescence images of platelet-decorated VWF fibers and platelet-VWF aggregates observed in microfluidic experiments at the indicated shear rates (*different columns*). Microfluidic channels were perfused with plasmatic wild-type VWF (wt-VWF, *top row*), VWF with the A2 domain deleted (ΔA2-VWF, *middle row*), or VWF with the A1 domain deleted (ΔA1-VWF, *bottom row*). A static image is presented as background, displaying platelets, fibers, and aggregates in black. Moving fibers and aggregates are highlighted in color. Their positions were tracked during 10 s after taking the static image. Flow direction is indicated with the arrow and the line corresponds to 100 μm. To see this figure in color, go online.

VWF-platelet aggregates independent of the VWF present in the perfusion medium.

DISCUSSION

Blockage of the GPIbα binding site mediated by A1-A2 interactions implies autoinhibition

Our extensive set of simulations (in the μs time range) demonstrates that the GPIbα binding site of VWF (located in the A1 domain) can be significantly blocked, upon spontaneous binding of the A2 to the A1 domain (Fig. 1). In addition, the binding of these two domains was further confirmed at the single-molecule level by AFM (Fig. 4). The increase in blockage with reducing interdomain separation observed in our simulations suggests that the A2 domain does not recognize a random region in the A1 domain but instead it specifically targets the GPIbα binding site. This observation was further supported by our docking calculations, which showed enrichment toward blocked conformations over random conformations, by enhanced shape complementarity and favorable protein-protein interactions (Fig. S5). With the GPIbα binding site blocked, platelets are prevented to bind and thus the VWF remains inactive. Our results, together with the experimentally observed platelet-binding modulation in the presence of A2 domains (30), thus imply an autoinhibition mechanism for the binding of platelets to the VWF mediated by A1-A2 interactions.

Additional simulations, this time with the two domains connected (also in the μs time range), revealed broad dynamics of the VWF-A1A2 fragment (Fig. S2). Although the A2 domain (bound to the A1 domain) was sometimes observed causing no shielding, presumably stabilized by the connecting linker, it was also found in many other times substantially blocking the GPIbα binding site. This indicates that not only not connected, but also vicinal, covalently linked, A1 and A2 domains can interact with each other causing blockage, further supporting the hypothesis of VWF autoinhibition because of A1-A2 interactions.

Our simulations of connected domains sampled a range from compact to extended conformations, covering the lower region of the interdomain separations measured by EM (6). In fact, compact conformations are expected from a direct A1-A2 interaction, as established in previous assays (30) and confirmed in our AFM experiments. Also, the presence of a third domain (e.g., D'D3 or A3) or deposition on the surface may favor more extended conformations in the EM experiments compared with the ones sampled in our simulations.

Autoinhibition driven by A1-A2 interactions provides a molecular picture of the shielding of the GPIbα (platelet) binding site, crucial to maintain the VWF inactive under equilibrium conditions. This is a complementary scenario to previous shear-dependent models (18,20) for GPIbα binding, but is the only one reconciling previous inactivation experiments (30).

Main orientational modes of the autoinhibited state

From our simulations, the minimum structural requirement to block GPIbα binding is to have A1-A2 binding and this is effectively achieved by the A2 domain specifically targeting the GPIbα binding site in A1. Our docking calculations and further extensive MD refinement narrowed the interdomain conformational variability to two main orientational modes of blockage, stabilized by an attractive interdomain potential energy and a reduction in the amount of solvent accessible hydrophobic surface (Fig. 2). A2 located either with its C terminus or with its β3 strand in proximity to the β3 strand of A1, resulting in a quasi-extended cross-domain β-sheet in the latter case. Notably, as a general feature, the A2 domain obstructs the A1-domain β3 strand (which connects to GPIbα (15,16)), thus suggesting drastic VWF autoinhibition. Direct blockage of the main interaction partner of GPIbα in the A1 domain (the β3 strand) was also observed in our simulations started from unbiased positions, with the domains separated, further supporting our proposed mode of autoinhibition. In addition, the agreement between our force-probe MD simulations and AFM experiments (see below) stresses on the validity of the chosen conformations from docking, followed by MD refinement, and the robustness of the MD simulation results. Our structural predictions are anticipated to motivate future structural studies aiming at determining the structure of the A1-A2 complex, in the nonconnected and connected situations, both of physiological relevance. Mutants Arg1668Asp, Asp1587Lys, and Val1548Ser(Asn) may serve as initial candidates for mutagenesis studies to discern among the two proposed modes of blockage.

In the simulations started from separated domains, additional blocking orientations were observed. Here, the presence of the N-linked sugars or the O-glycosylated linker may also play stabilization roles. An additional stabilization of the blocked (autoinhibited) state of the VWF by the sugars is consistent with recent microfluidic experiments that showed an increase in platelet adhesion when the VWF was N-deglycosylated (46).

Force unblocks the GPIbα-binding site before exposure of the ADAMTS13 cleavage site, ensuring VWF activation before cleavage

In our force-probe simulations, we induced the dissociation of the complex formed by the A1 and A2 domains by applying an external stretching force. In complex, the VWF A2 domain showed only marginal unfolding, which proceeded from the C terminus, in line with the unfolding mechanism previously observed for this domain in isolation (with different force fields) (23,47). Dissociation was found to occur before exposure of the ADAMTS13 cleavage site in the A2 domain with a very high probability (~0.88) (Fig. 3).

This is consistent with our AFM measurements, which yielded in the majority of the binding events small elongations of the VWF-A1A2 complex at rupture (Fig. 4). Our simulations and AFM thus support that a stretching force unblocks the GPIbα-binding site, by detaching the A1 and A2 domains, and that this process is coupled to the exposure of the ADAMTS13 cleavage site in the A2 domain after its unfolding. The stretching force ensures, however, that the VWF is activated for platelet binding predominantly before deactivation through cleavage. In this respect, the interactions between A1 and A2 may also serve to clarify the role of ristocetin, coupling platelet binding and ADAMTS13 cleavage (48).

Deletion of the A2 domain results in a VWF with a gain of function

Our microfluidic experiments showed a reduction of the critical shear-rate for the formation of VWF-platelet fibers and rolling aggregates, when the A2 domain was deleted. This implies a VWF with a gain in function (Fig. 5). Our results in consequence expand the experiments by Martin et al. (30), proving that not only present in solution but also within the VWF molecule, the A2 domain critically influences platelet binding in a shear-dependent manner. In addition, our combined computational and experimental results suggest that the A2 domain stabilizes a VWF inactive state, by direct A1-A2 interactions, either within or across VWF monomers. However, additional inhibitory mechanisms must be at play, because the ΔA2-VWF mutant still requires intermediate shear rates for the formation of rolling aggregates (2500 s^{-1} for ΔA2-VWF instead of 4000 s^{-1} for the wild-type VWF). We speculate that the exposure of the GPIbα binding site requires both a global globule-to-stretch transition, eventually involving other—specific or nonspecific—domain-domain interactions (e.g., between D'D3 and A1 (28)), and VWF-A1A2 dissociation.

CONCLUSIONS

In this study, we examined the inactivation of VWF for platelet binding, induced by a specific domain-domain interaction, and its coupling to VWF cleavage degradation driven by force, by using MD simulations, molecular docking, AFM, and microfluidic experiments. We demonstrate that under equilibrium conditions the VWF A1 and A2 domains bind to each other, with the A2 domain specifically targeting the GPIbα binding site in the A1 domain, thus blocking the binding of GPIbα (and thereby of platelets) to VWF. This implies autoinhibition of the VWF mediated by A1-A2 interactions. We identified two main orientational blocking modes, which have the shielding of the A1 β3 strand, the site critical for GPIbα binding, in common. Detachment of the two domains, induced by a stretching force, unblocked the GPIbα binding site most predominantly before exposure of the cleavage site in the A2 domain. This suggests that A2 blocks GPIbα binding in a force-dependent manner, but guaranteeing that the VWF is ready for activation before cleavage, to mechanically balance the propagation and attenuation of hemostasis. Deletion of the A2 domain enhanced platelet binding, corroborating the key autoinhibition role of this domain. In summary, our results suggest, to our knowledge, a new interdomain-mediated autoinhibition mechanism that explains the inactivation of VWF under equilibrium conditions while allowing shear-sensitive growth of blood coagulates. This mechanism reconciles previous and can be tested by future experiments. It will be highly interesting to investigate if this or other domain-domain interactions are a common regulatory mechanism, not only for the shear-sensitive binding of VWF to its partners, but also potentially for the shear-dependent self-aggregation of VWF.

SUPPORTING MATERIAL

Supporting Materials and Methods, seven figures, and one movie are available at http://www.biophysj.org/biophysj/supplemental/S0006-3495(15)00302-1.

AUTHOR CONTRIBUTIONS

C.A.-S. performed the MD simulations and docking calculations with Patchdock and Firedock. C.A.-S., C.B., and F.G. analyzed the computational results. V.H., S.G., and S.W.S. performed the microfluidic experiments. S.P. and P.H. carried out the AFM experiments. A.K.B. performed the docking calculations with RosettaDock. M.A.B., T.O., and R.S. generated the VWF constructs. C.B. and F.G. conceived the project. All authors discussed the results. C.A.-S., V.H., S.P., A.K.B., M.A.B., C.B., and F.G. wrote the manuscript.

ACKNOWLEDGMENTS

This study was supported by research funding from the German Research Foundation, to the Research Group FOR1543: "Shear flow regulation of hemostasis—bridging the gap between nanomechanics and clinical presentation" (C.A.-S., V.H., S.P., S.G., M.A.B., T.O., R.S., P.H., S.W.S., C.B., and F.G.), the Klaus Tschira Stiftung (F.G.), and the BIOMS program of the Heidelberg University (A.K.B.). We thank the Jülich Supercomputing Centre (J.S.C.) (HHD24 and HHD25 projects). We thank Gesa König for technical assistance with protein purification.

SUPPORTING CITATIONS

References (49–74) appear in the Supporting Material.

REFERENCES

1. Schneppenheim, R., and U. Budde. 2011. von Willebrand factor: the complex molecular genetics of a multidomain and multifunctional protein. *J. Thromb. Haemost.* 9 (*Suppl. 1*):209–215.
2. Springer, T. A. 2011. Biology and physics of von Willebrand factor concatamers. *J. Thromb. Haemost.* 9 (*Suppl. 1*):130–143.
3. Chen, H., M. A. Fallah, …, A. Alexander-Katz. 2013. Blood-clotting-inspired reversible polymer—colloid composite assembly in flow. *Nat. Commun.* 4:1333. http://dx.doi.org/10.1038/ncomms2326.

4. Lippok, S., T. Obser, …, J. O. Rädler. 2013. Exponential size distribution of von Willebrand factor. *Biophys. J.* 105:1208–1216.
5. Schneider, S. W., S. Nuschele, …, M. F. Schneider. 2007. Shear-induced unfolding triggers adhesion of von Willebrand factor fibers. *Proc. Natl. Acad. Sci. USA.* 104:7899–7903.
6. Zhou, Y.-F., E. T. Eng, …, T. A. Springer. 2011. A pH-regulated dimeric bouquet in the structure of von Willebrand factor. *EMBO J.* 30:4098–4111.
7. Zhou, Y.-F., E. T. Eng, …, T. A. Springer. 2012. Sequence and structure relationships within von Willebrand factor. *Blood.* 120:449–458.
8. Alexander-Katz, A., M. F. Schneider, …, R. R. Netz. 2006. Shear-flow-induced unfolding of polymeric globules. *Phys. Rev. Lett.* 97:138101.
9. Sing, C. E., and A. Alexander-Katz. 2010. Elongational flow induces the unfolding of von Willebrand factor at physiological flow rates. *Biophys. J.* 98:L35–L37.
10. Sing, C. E., J. G. Selvidge, and A. Alexander-Katz. 2013. Von Willlebrand adhesion to surfaces at high shear rates is controlled by long-lived bonds. *Biophys. J.* 105:1475–1481.
11. Emsley, J., M. Cruz, …, R. Liddington. 1998. Crystal structure of the von Willebrand factor A1 domain and implications for the binding of platelet glycoprotein Ib. *J. Biol. Chem.* 273:10396–10401.
12. Zhang, Q., Y.-F. Zhou, …, T. A. Springer. 2009. Structural specializations of A2, a force-sensing domain in the ultralarge vascular protein von Willebrand factor. *Proc. Natl. Acad. Sci. USA.* 106:9226–9231.
13. Zhou, M., X. Dong, …, J. Ding. 2011. A novel calcium-binding site of von Willebrand factor A2 domain regulates its cleavage by ADAMTS13. *Blood.* 117:4623–4631.
14. Xu, A. J., and T. A. Springer. 2012. Calcium stabilizes the von Willebrand factor A2 domain by promoting refolding. *Proc. Natl. Acad. Sci. USA.* 109:3742–3747.
15. Huizinga, E. G., S. Tsuji, …, P. Gros. 2002. Structures of glycoprotein Ibalpha and its complex with von Willebrand factor A1 domain. *Science.* 297:1176–1179.
16. Dumas, J. J., R. Kumar, …, L. Mosyak. 2004. Crystal structure of the wild-type von Willebrand factor A1-glycoprotein Ibalpha complex reveals conformation differences with a complex bearing von Willebrand disease mutations. *J. Biol. Chem.* 279:23327–23334.
17. Chen, Z., J. Lou, …, K. Schulten. 2008. Flow-induced structural transition in the beta-switch region of glycoprotein Ib. *Biophys. J.* 95:1303–1313.
18. Lou, J., and C. Zhu. 2008. Flow induces loop-to-beta-hairpin transition on the beta-switch of platelet glycoprotein Ib α. *Proc. Natl. Acad. Sci. USA.* 105:13847–13852.
19. Zou, X., Y. Liu, …, K. Schulten. 2010. Flow-induced beta-hairpin folding of the glycoprotein Ibalpha beta-switch. *Biophys. J.* 99:1182–1191.
20. Kim, J., C.-Z. Zhang, …, T. A. Springer. 2010. A mechanically stabilized receptor-ligand flex-bond important in the vasculature. *Nature.* 466:992–995.
21. Blenner, M. A., X. Dong, and T. A. Springer. 2014. Structural basis of regulation of von Willebrand factor binding to glycoprotein Ib. *J. Biol. Chem.* 289:5565–5579.
22. Sadler, J. E. 2002. A new name in thrombosis, ADAMTS13. *Proc. Natl. Acad. Sci. USA.* 99:11552–11554.
23. Baldauf, C., R. Schneppenheim, …, F. Gräter. 2009. Shear-induced unfolding activates von Willebrand factor A2 domain for proteolysis. *J. Thromb. Haemost.* 7:2096–2105.
24. Chen, W., J. Lou, and C. Zhu. 2009. Molecular dynamics simulated unfolding of von Willebrand factor A domains by force. *Cell Mol. Bioeng.* 2:75–86.
25. Zhang, X., K. Halvorsen, …, T. A. Springer. 2009. Mechanoenzymatic cleavage of the ultralarge vascular protein von Willebrand factor. *Science.* 324:1330–1334.
26. Wu, T., J. Lin, …, C. Zhu. 2010. Force-induced cleavage of single VWFA1A2A3 tridomains by ADAMTS-13. *Blood.* 115:370–378.
27. Ying, J., Y. Ling, …, J.-Y. Shao. 2010. Unfolding the A2 domain of von Willebrand factor with the optical trap. *Biophys. J.* 98:1685–1693.
28. Ulrichts, H., M. Udvardy, …, H. Deckmyn. 2006. Shielding of the A1 domain by the D'D3 domains of von Willebrand factor modulates its interaction with platelet glycoprotein Ib-IX-V. *J. Biol. Chem.* 281:4699–4707.
29. Auton, M., K. E. Sowa, …, M. A. Cruz. 2012. N-terminal flanking region of A1 domain in von Willebrand factor stabilizes structure of A1A2A3 complex and modulates platelet activation under shear stress. *J. Biol. Chem.* 287:14579–14585.
30. Martin, C., L. D. Morales, and M. A. Cruz. 2007. Purified A2 domain of von Willebrand factor binds to the active conformation of von Willebrand factor and blocks the interaction with platelet glycoprotein Ibalpha. *J. Thromb. Haemost.* 5:1363–1370.
31. Lenting, P. J., and C. V. Denis. 2007. von Willebrand factor A1 domain: stuck in the middle. *J. Thromb. Haemost.* 5:1361–1362.
32. Canis, K., T. A. J. McKinnon, …, A. Dell. 2010. The plasma von Willebrand factor O-glycome comprises a surprising variety of structures including ABH antigens and disialosyl motifs. *J. Thromb. Haemost.* 8:137–145.
33. Matsui, T., K. Titani, and T. Mizuochi. 1992. Structures of the asparagine-linked oligosaccharide chains of human von Willebrand factor. Occurrence of blood group A, B, and H(O) structures. *J. Biol. Chem.* 267:8723–8731.
34. Van Der Spoel, D., E. Lindahl, …, H. J. C. Berendsen. 2005. GROMACS: fast, flexible, and free. *J. Comput. Chem.* 26:1701–1718.
35. Hess, B., C. Kutzner, …, E. Lindahl. 2008. GROMACS 4: algorithms for highly efficient, load-balanced, and scalable molecular simulation. *J. Chem. Theory Comput.* 4:435–447.
36. Pronk, S., S. Páll, …, E. Lindahl. 2013. GROMACS 4.5: a high-throughput and highly parallel open source molecular simulation toolkit. *Bioinformatics.* 29:845–854.
37. Amadei, A., A. B. M. Linssen, and H. J. C. Berendsen. 1993. Essential dynamics of proteins. *Proteins Struct. Funct. Bioinformatics.* 17: 412–425.
38. Schneidman-Duhovny, D., Y. Inbar, …, H. J. Wolfson. 2005. PatchDock and SymmDock: servers for rigid and symmetric docking. *Nucleic Acids Res.* 33:W363–W367.
39. Mashiach, E., D. Schneidman-Duhovny, …, H. J. Wolfson. 2008. FireDock: a web server for fast interaction refinement in molecular docking. *Nucleic Acids Res.* 36 (*Suppl. 2*):W229–W332.
40. Lyskov, S., and J. J. Gray. 2008. The RosettaDock server for local protein-protein docking. *Nucleic Acids Res.* 36 (*Suppl. 2*):W233–W238.
41. Schneppenheim, R., J. J. Michiels, …, U. Budde. 2010. A cluster of mutations in the D3 domain of von Willebrand factor correlates with a distinct subgroup of von Willebrand disease: type 2A/IIE. *Blood.* 115:4894–4901.
42. Schneppenheim, R., U. Budde, …, J. Oldenburg. 2001. Expression and characterization of von Willebrand factor dimerization defects in different types of von Willebrand disease. *Blood.* 97:2059–2066.
43. Grässle, S., V. Huck, …, S. W. Schneider. 2014. von Willebrand factor directly interacts with DNA from neutrophil extracellular traps. *Arterioscler. Thromb. Vasc. Biol.* 34:1382–1389.
44. Kienberger, F., V. P. Pastushenko, …, P. Hinterdorfer. 2000. Static and dynamical properties of single poly(ethylene glycol) molecules investigated by force spectroscopy. *Single Molecules.* 1:123–128.
45. Brehm, M. A., V. Huck, …, R. Schneppenheim. 2014. von Willebrand disease type 2A phenotypes IIC, IID and IIE: a day in the life of shear-stressed mutant von Willebrand factor. *Thromb. Haemost.* 112:96–108.
46. Fallah, M. A., V. Huck, …, M. F. Schneider. 2013. Circulating but not immobilized N-deglycosylated von Willebrand factor increases platelet adhesion under flow conditions. *Biomicrofluidics.* 7:044124.
47. Interlandi, G., M. Ling, …, W. E. Thomas. 2012. Structural basis of type 2A von Willebrand disease investigated by molecular dynamics simulations and experiments. *PLoS ONE.* 7:e45207.

48. Chen, J., M. Ling, …, D. W. Chung. 2012. Simultaneous exposure of sites in von Willebrand factor for glycoprotein Ib binding and ADAMTS13 cleavage: studies with ristocetin. *Arterioscler. Thromb. Vasc. Biol.* 32:2625–2630.

49. Woods Group. 2005–2013. GLYCAM Web. *In* R. J. Woods, editor. Complex Carbohydrate Research Center, University of Georgia, Athens, GA.

50. Schrödinger, L. L. C. 2010. The PyMOL Molecular Graphics System, Version 1.3r1.

51. Hornak, V., R. Abel, …, C. Simmerling. 2006. Comparison of multiple Amber force fields and development of improved protein backbone parameters. *Proteins Struct. Funct. Bioinformatics.* 65:712–725.

52. Best, R. B., and G. Hummer. 2009. Optimized molecular dynamics force fields applied to the helix-coil transition of polypeptides. *J. Phys. Chem. B.* 113:9004–9015.

53. Lindorff-Larsen, K., S. Piana, …, D. E. Shaw. 2010. Improved side-chain torsion potentials for the Amber ff99SB protein force field. *Proteins Struct. Funct. Bioinformatics.* 78:1950–1958.

54. Kirschner, K. N., A. B. Yongye, …, R. J. Woods. 2008. GLYCAM06: a generalizable biomolecular force field. Carbohydrates. *J. Comput. Chem.* 29:622–655.

55. Jorgensen, W. L., J. Chandrasekhar, …, M. L. Klein. 1983. Comparison of simple potential functions for simulating liquid water. *J. Chem. Phys.* 79:926–935.

56. Joung, I. S., and T. E. Cheatham, 3rd. 2008. Determination of alkali and halide monovalent ion parameters for use in explicitly solvated biomolecular simulations. *J. Phys. Chem. B.* 112:9020–9041.

57. Hess, B., H. Bekker, …, J. G. E. M. Fraaije. 1997. LINCS: a linear constraint solver for molecular simulations. *J. Comput. Chem.* 18:1463–1472.

58. Feenstra, K. A., B. Hess, and H. J. C. Berendsen. 1999. Improving efficiency of large timescale molecular dynamics simulations of hydrogen-rich systems. *J. Comput. Chem.* 20:786–798.

59. Miyamoto, S., and P. A. Kollman. 1992. Settle: an analytical version of the SHAKE and RATTLE algorithm for rigid water models. *J. Comput. Chem.* 13:952–962.

60. Hockney, R. W., and J. W. Eastwood. 1988. Computer Simulation Using Particles. Hilger, Bristol, UK.

61. Darden, T., D. York, and L. Pedersen. 1993. Particle mesh Ewald: an $N \cdot \log(N)$ method for Ewald sums in large systems. *J. Chem. Phys.* 98:10089–10092.

62. Essmann, U., L. Perera, …, L. G. Pedersen. 1995. A smooth particle mesh Ewald method. *J. Chem. Phys.* 103:8577–8593.

63. Bussi, G., D. Donadio, and M. Parrinello. 2007. Canonical sampling through velocity rescaling. *J. Chem. Phys.* 126:014101.

64. Berendsen, H. J. C., J. P. M. Postma, …, J. R. Haak. 1984. Molecular dynamics with coupling to an external bath. *J. Chem. Phys.* 81:3684–3690.

65. Parrinello, M., and A. Rahman. 1981. Polymorphic transitions in single crystals: a new molecular dynamics method. *J. Appl. Phys.* 52:7182–7190.

66. Connolly, M. L. 1983. Analytical molecular surface calculation. *J. Appl. Cryst.* 16:548–558.

67. Budde, U., R. Schneppenheim, …, I. Peake. 2008. Detailed von Willebrand factor multimer analysis in patients with von Willebrand disease in the European study, molecular and clinical markers for the diagnosis and management of type 1 von Willebrand disease (MCMDM-1VWD). *J. Thromb. Haemost.* 6:762–771.

68. Budde, U., R. Schneppenheim, …, T. S. Zimmerman. 1990. Luminographic detection of von Willebrand factor multimers in agarose gels and on nitrocellulose membranes. *Thromb. Haemost.* 63:312–315.

69. Schneppenheim, R., H. Plendl, and U. Budde. 1988. Luminography—an alternative assay for detection of von Willebrand factor multimers. *Thromb. Haemost.* 60:133–136.

70. Johannes Kepler University Linz. Crosslinkers and protocols for AFM tip functionalization. Published online April 8, 2015. http://www.jku.at/biophysics/content/e257042.

71. Hutter, J. L., and J. Bechhoefer. 1993. Calibration of atomic-force microscope tips. *Rev. Sci. Instrum.* 64:1868–1873.

72. Ebner, A., P. Hinterdorfer, and H. J. Gruber. 2007. Comparison of different aminofunctionalization strategies for attachment of single antibodies to AFM cantilevers. *Ultramicroscopy.* 107:922–927.

73. Zhu, R., S. Howorka, …, P. Hinterdorfer. 2010. Nanomechanical recognition measurements of individual DNA molecules reveal epigenetic methylation patterns. *Nat. Nanotechnol.* 5:788–791.

74. Rickham, P. P. 1964. Human experimentation: code of ethics of World Medical Association. Declaration of Helsinki. *BMJ.* 2:177.

Supporting material for

Force-sensitive autoinhibition of the von Willebrand factor mediated by inter-domain interactions

Camilo Aponte-Santamaría[†], Volker Huck[‡], Sandra Posch[§], Agnieszka K. Bronowska[†], Sandra Grässle[‡], Maria A. Brehm[¶], Tobias Obser[¶], Reinhard Schneppenheim[¶], Peter Hinterdorfer[§], Stefan W. Schneider[‡], Carsten Baldauf[||], and Frauke Gräter[†]

[†]Molecular Biomechanics Group, Heidelberg Institute for Theoretical Studies, Heidelberg, Germany
[‡]Experimental Dermatology, Medical Faculty Mannheim, Heidelberg University, Mannheim, Germany
[§]Department of Applied Experimental Biophysics, Institute of Biophysics, Johannes Kepler University, Linz, Austria
[¶]Department of Pediatric Hematology and Oncology, University Medical Center Hamburg-Eppendorf, Hamburg, Germany
[||]Theory Department, Fritz-Haber-Institut der Max-Planck-Gesellschaft, Berlin, Germany

Supporting figures

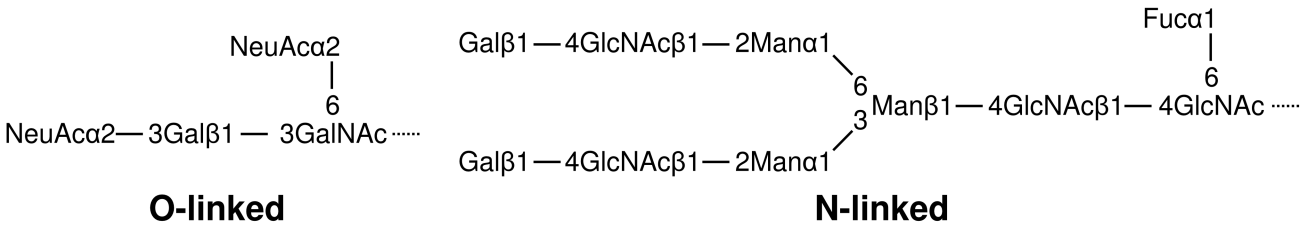

Figure S1. O-linked (left) and N-linked (right) sugars used in the molecular dynamics (MD) simulations of the von Willebrand factor (VWF) A1 and A2 domains. They were attached to the side chains of the glycosylated residues highlighted in Fig. 1A in the main text. They are the two most predominant sugars bound to VWF, accounting for 62.5 % of the O-linked and 59.9 % of the N-linked sugars.

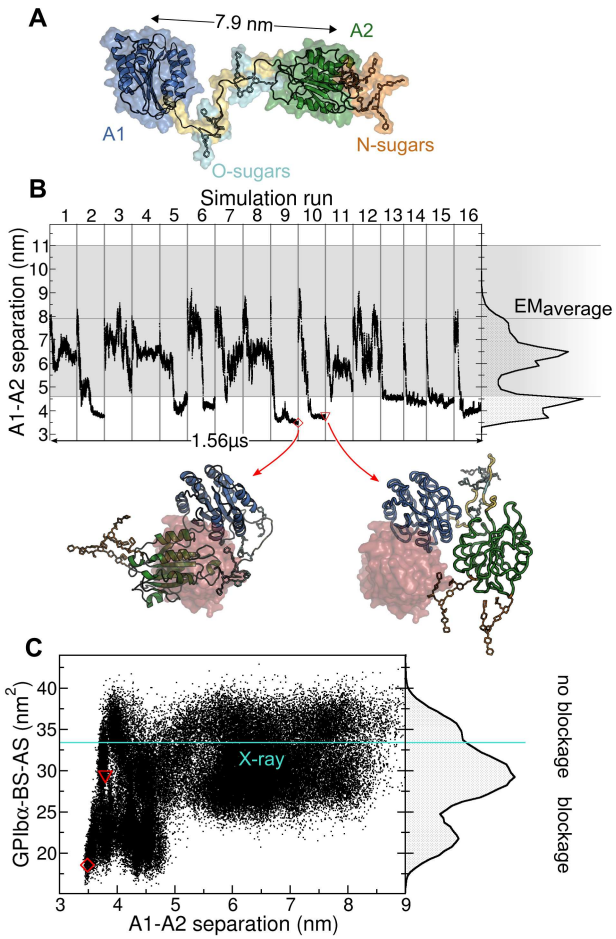

Figure S2. Blockage of the GPIbα binding site in the von Willebrand factor (VWF) revealed by molecular dynamics (MD) simulations of the VWF-A1A2 fragment, including the inter-domain linker. A. Typical starting conformation used in the MD simulations (protein as cartoon and surface, and sugars as sticks). Residues 1269 to 1670 of the human VWF were considered. The A1 (blue) and A2 (green) domains are connected by a 30 residue linker (yellow). Four O-linked sugars (O-sugars, cyan) are located at the linker and two N-linked sugars (N-sugars, orange) at the A2 domain. The initial domain-domain center of mass (A1-A2) separation is indicated with the black arrow. Multiple inter-domain starting orientations were considered. **B.** A1-A2 separation along the concatenated MD simulation time. Gray lines separate individual MD runs. Right plot displays the normalized histogram of the The A1-A2 separation. The range of separations observed by electron microscopy (1) is depicted in gray (average, minimum and maximum highlighted with the horizontal lines). Conformations at the bottom show examples, with the two domains in contact (cartoon) contrasted to the region occupied by GPIbα when it binds to A1 (red surface), taken at the instants marked with the open red symbols. **C.** GPIbα binding site accessible surface (GPIbα-BS-AS) as a function of the A1-A2 separation (main panel) and its normalized histogram (right plot). Reduced GPIbα-BS-AS values correspond to blockage of the GPIbα binding site. The GPIbα-BS-AS derived from the VWF A1-GPIbα complex X-ray structure (2) is indicated by the cyan line. The open symbols correspond to the conformations shown at the bottom of B.

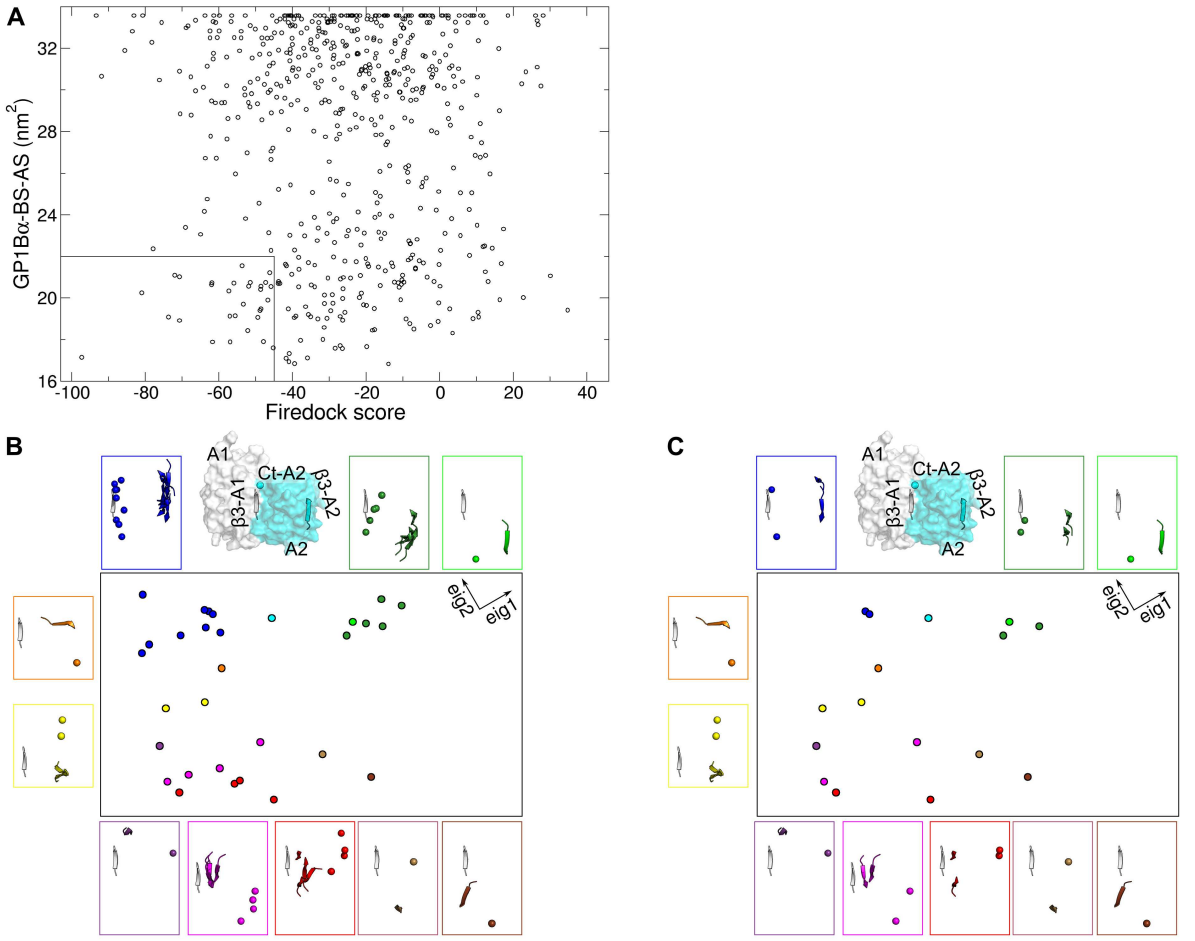

Figure S3. Docking of von Willebrand factor (VWF) A2 domain to the VWF A1 domain, resulting in blockage of the GP1Bα binding site. A. A set of conformations with the A1 and A2 domains of the VWF in contact with each other was generated by using Patchdock and refined using Firedock. For the resulting conformations, the GP1Bα binding site accessible surface (GP1Bα-BS-AS) is plotted as a function of the Firedock ranking score. The conformations presenting both substantial blockage and high Firedock scores (laying in the square at the lower left corner) were selected. **B.** Conformations were clustered based on their RMSD yielding 11 groups (different colors). The orientations belonging to each group are displayed in the colored boxes (with the β3 strand in cartoon and the C-terminus of the A2 domain in sphere representation, and the A1 domain in white and the A2 domain in color). The protein surface is also depicted for the group colored with cyan. A principal component analysis (PCA) considering this set of conformations yielded two principal collective vectors eig1 and eig2 (which together accounted for 68 % of the inter-domain orientational changes). Conformations were projected onto the 2-dimensional (2D) space constituted by these two vectors in the black square (each circle represents one conformation), confirming the clustering between conformations. **C.** From each group the two (or one in the case of only one) conformations with highest Firedock ranking scores were selected as the starting positions for the MD simulations presented in Fig. 2A in the main text. Their orientations and projections (onto the 2D PCA space created by all the conformations) are shown here (with the same format as in B). See further details of the docking procedure in the supporting text. In B and C projections are in arbitrary units.

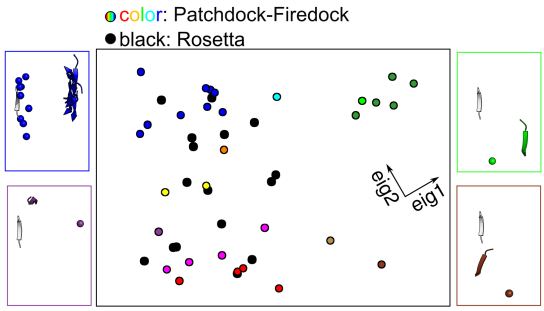

Figure S4. Comparison between Patchdock-Firedock and Rosetta molecular docking. Projections of the conformations of the von Willebrand factor (VWF) A1 and A2 domains, in contact and blocking the GP1Bα binding site, predicted by Patchdock and Firedock (color) compared to the ones predicted by Rosetta (black). Projections were done onto 2-dimensional Patchdock and Firedock principal component space (presented in Fig. S3), with each circle representing one conformation. Overlap between projections indicate similar predictions by the two docking methodologies. To facilitate the comparison, the conformations associated to some projections are illustrated in the colored squares (with the β3 strands in cartoon and the C-terminus of the VWF A2 domain in sphere representation, and with VWF A1 in white and VWF A2 in the same color as in the projections). Projections are in arbitrary units.

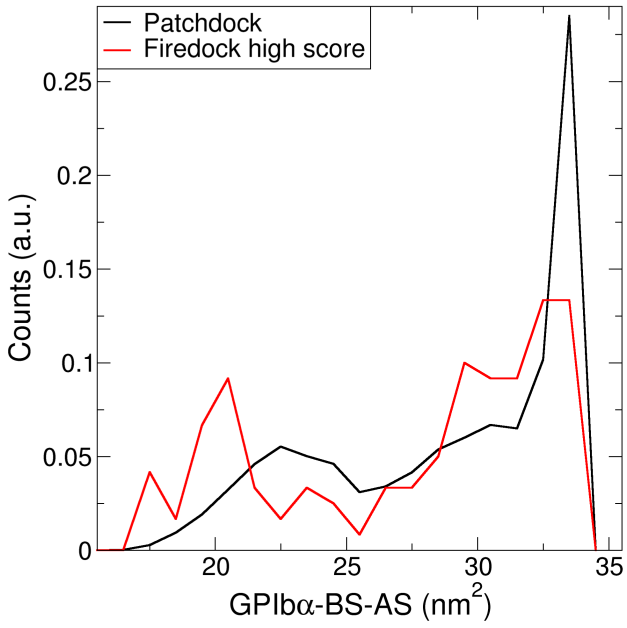

Figure S5. Distribution of the GPIbα binding site accessible surface (GP1Bα-BS-AS) for all possible poses predicted by Patchdock and for the ones with high Firedock score.

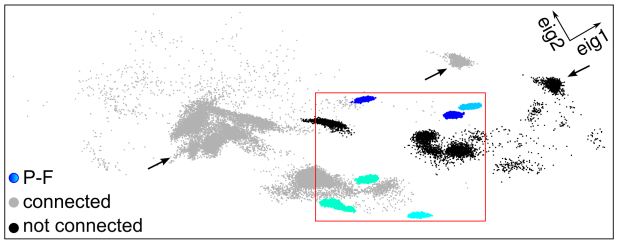

Figure S6. Comparison between orientations extracted from different simulations of the von Willebrand factor (VWF) A1 and A2 domains, in contact and blocking the GP1Bα binding site. Projections onto the 2-dimensional Patchdock and Firedock (P-F) principal component space (presented in Fig. S3), with each circle representing one conformation. Projections of the refined docking-MD set (presented in Fig. 2 of the main text) are shown in color. Projections from trajectories starting from connected and separated domains are displayed in gray (set from Fig. S2), and from not connected and separated domains in black (set from Fig. 1). The red square indicates the extent of the refined docking-MD data set, with the A2 domain situated directly in front of the β3 strand of the A1 domain, which was also covered by the other two data sets. The arrows point to regions populated only in the simulations starting with separated domains. Projections in arbitrary units.

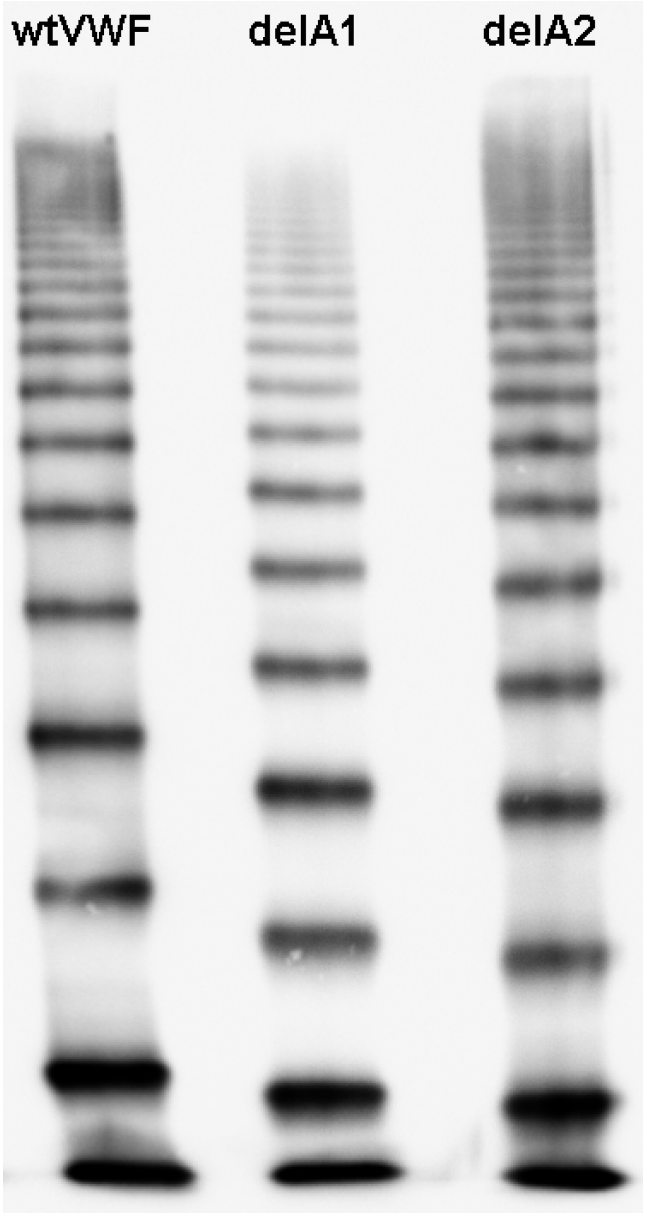

Figure S7. Multimer analysis of recombinant VWF. Multimer analysis of recombinant wild-type VWF (wtVWF) and deletion mutants lacking either the A1 (delA1) or the A2 (delA2) domain was performed by SDS agarose electrophoresis gels and immunoblotting onto nitrocellulose membrane with luminescent visualisation.

Supporting video S1

Comparison of flow through microfluidic channels, perfused with wild-type VWF (upper channel) versus VWF with the A2 domain deleted (lower channel). (Minute 1) Shear is maintained constant at $500\,s^{-1}$. Here, rolling of single platelets is observed for both proteins. (Minute 2-4) Shear is kept fixed at $2500\,s^{-1}$. Large rolling aggregates, formed by platelets and VWF, are observed for the VWF lacking the A2 domain (lower channel), while only reversibly formed platelet-decorated VWF fibers, which stayed attached to the channel surface are observed for wild-type VWF (upper channel). (Minute 5-end of the movie) Shear is retained at a value of $4000\,s^{-1}$. Large aggregates are formed for both proteins. Frames were taken at a frequency of 2 frames per second. Time is indicated in seconds the first minute and in minutes after. The white bar corresponds to $100\,\mu$m. Platelets and VWF are shown in white.

Supporting text

1 Molecular dynamics (MD) simulations

1.1 Equilibrium MD simulations of not connected von Willebrand factor (VWF) A1 and A2 domains

The starting atomic positions of the A1 and A2 domains were taken from their X-ray structures (PDB ids. 1AUQ (3) and 3GXB (4), respectively). The two domains were initially separated by distances (between center of masses) varying from 6.1 nm to 8.6 nm. The N-linked sugars considered for the simulations are shown in Fig. S1. They account for 59.9 % of the N-linked (5) sugars bound to VWF. Their atomic coordinates were obtained with the Glycoprotein web server GLYCAM-Web (www.glycam.org) (6). They were attached to Asn1515 and to Asn1574, in the A2 domain. For the attachment, the sugars were aligned to the side chain of the residues, using PyMOL (7) and the *g_confrms* tool of the GROMACS package (8–10), ensuring that there were no steric clashes neither with other sugars nor with the protein. Internal disulfide bonds observed in the X-ray structures (3, 4) were imposed between the cysteine pairs Cys1272-Cys1458 in the A1 domain and Cys1669-Cys1670 in the A2 domain. The two domains were solvated by ∼121000 water molecules, and sodium and chloride ions (∼150 mM concentration) in a dodecahedron box. Additional sodium ions were added to maintain the system electrically neutral. An energy minimization step and a simulation of 1 ns, equilibrating the solvent with all the heavy atoms of the complex harmonically restrained, preceded the production runs. 17 independent 100 ns MD simulations, with different starting inter-domain orientations, were carried out, yielding $1.7\,\mu$s concatenated simulation time. See Section 1.4 below for the used force field, and algorithms and parameters employed during the energy minimization, solvent equilibration, system neutralization, and MD simulations.

In addition, 16 MD simulations of 100 ns each ($1.6\,\mu$s concatenated time), starting with the two domains in contact forming a complex were carried out. The starting structures of the complex

were obtained by docking the structures of A1 and A2 using Patchdock (11) and refined using Firedock (12). See details of the docking procedure in Section 4 and selection of starting conformations in Fig. S3. Same simulation parameters as above were used, except for a smaller simulation box containing 24000 to 55000 water molecules and a longer solvent equilibration of 10 ns (with the N-linked sugars also free to move).

1.2 Equilibrium MD simulations of connected VWF A1 and A2 domains

MD simulations of the VWF-A1A2 fragment (residues 1269 to 1670 of the VWF sequence), consisting of the A1 and A2 domains connected by a 30 amino acid linker, were carried out. Starting structures of the domains were the same as in the simulations of the unconnected A1 and A2 domains (Section 1.1), but here, the two domains were separated by a distance (between center of masses) of 7.9 nm, corresponding to the average separation observed in electron microscopy (EM) images (1). In addition to the N-linked sugars attached to the A2 domain, the O-linked sugar accounting for 62.5 % of the VWF O-glycome (13) (Fig. S1) was appended to the linker at residues Thr1468, Thr1477, Ser1486 and Thr1487. Atomic coordinates for the O-linked sugars were obtained with the Glycoprotein web server GLYCAM-Web (www.glycam.org) (6), and the same attachment procedure was applied as for the N-linked sugars in Section 1.1. To generate the initial conformation of the linker, a 50 ns equilibrium MD simulation, starting from a completely stretched, fully solvated and O-linked glycosylated linker, was carried out. From this simulation, a conformation with an end to end distance of 6.0 nm (in accordance to the EM estimates (1)) was selected. Next, the domains were placed at different orientations, and connected by the resulting 6 nm linker. 16 independent MD simulations, with lengths from 82 ns to 100 ns (for $\sim 1.56\mu$s concatenated simulation time), were carried out. They were preceded by the following equilibration steps. First, the fragment was placed in a cubic box containing approximately 53000 water molecules and sodium and chloride ions at $\sim$150 mM concentration, with an excess of sodium ions to keep the system electrically neutral. Second, the system was energy minimized. Third, the solvent was equilibrated during 1 ns, with the protein harmonically restrained. Fourth, the linker was equilibrated during 10 ns, by releasing its restraints, but still maintaining the A1 and A2 domains harmonically fixed. Fifth, to allow full rotation, the fragment was accommodated in a larger dodecahedron box, which contained approximately 135000 water molecules. Sixth, the solvent was equilibrated in the new box during 500 ps, with the fragment harmonically restrained. Finally, restrains on the fragment were released. The used force field, and simulation algorithms and parameters are described in detail in Section 1.4 below.

1.3 Force-probe MD simulations

Force-probe simulations of not connected A1 and A2 domains forming a complex were performed by exerting an external harmonic force F_1 on the N-terminus of the A1 domain and F_2 on the C-terminus of the A2 domain. Harmonic springs (with elastic constants K =500 kJmol^{-1}nm^{-2}) were attached to these termini, and were moved away from each other along the x axis at a constant

pulling velocity, V, of 0.2 m/s. Harmonic forces (acting along the x-axis) were computed as

$$F_i(t) = -K\left[x_i(t) - x_i(0) - V_i t\right], \quad i = 1, 2. \tag{1}$$

Here, $x_i(t)$ is the terminus x-coordinate ($i = 1$ for the A1 N-terminus and $i = 2$ for the A2 C-terminus) at time t. The harmonic spring attached to the A1 N-terminus was moved at velocity $V_1 = -V/2$ and the one attached to the A2 C-terminus at velocity $V_2 = V/2$.

Simulations were started from 17 different starting conformations. One conformation was extracted from one of the equilibrium simulations of the two domains showing spontaneous binding (run number 8 in Fig. 1C of main text). The remaining 16 corresponded to a representative conformations extracted from the equilibrium MD simulations of the A1 and A2 domains forming a complex. For each run, the complex was aligned along the x axis and centered in a cubic box of water solvent and sodium and chloride ions at ∼150 mM concentration. The box dimensions were approximately the diameter of the complex, adding 11.5 nm in the x-axis and 1.5 nm in the y- and z-axis, to provide enough space to accommodate the stretched fragments of the protein. Extra sodium ions were added to neutralize the net charge of the protein. The system was energy minimized and the solvent was equilibrated for 1 ns (with the protein harmonically restrained).

Simulations were continued until the complex dissociated. For two cases, the springs reached the box walls in the x-axis and the domains were still in complex. For these two cases, force probe MD simulations were continued without increasing the simulation box size, after deleting the unfolded C-terminal part of the A2 domain (20 residues in one and 21 residues the other case). It was ensured that the deleted portion was almost fully stretched and that the tensile force was nearly zero at the moment of deletion, thereby causing a minimum effect on the elastic constant of the pulling springs. The remaining part of the complex was re-centered in the box, energy minimized, solvent equilibrated for 500 ps (with the protein harmonically restrained), and subjected to harmonic forces, starting with the same forces on the termini as at the moment of deletion.

The used force field, and the algorithms and parameters for energy minimization, solvent equilibration, system neutralization, and MD simulations are presented in Section 1.4 below.

1.4 Force field and MD simulation parameters

In addition to water molecules, sodium and chloride ions (at 150 mM concentration) and an excess of sodium ions to keep the system electrically neutral were always added to the system. All simulations were carried out with the GROMACS package (8–10, 14) (4.5.5 version). The Amber99sb-ildn* force field (15–17) was used for the protein, GLYCAM06 parameters for the sugars (18), the TIP3P model (19) for the water molecules, and parameters determined by Joung *et al.* (20) for the ions. Energy minimizations were carried out with the steepest descent algorithm. Solvent equilibration simulations were carried out with the protein heavy atoms harmonically restrained (harmonic force constant of 1000 $\mathrm{kJmol^{-1}nm^{-2}}$). Constraints were imposed over all bonds by using the LINCS algorithm (21) and virtual interaction-sites were added to take into account fast angular motions

involving hydrogen atoms (22). For the water molecules, both bond lengths and angles were constrained by means the Settle algorithm (23). The use of these bond and angular constraint algorithms allowed to integrate Newtonian equations of motion by using of the leap frog algorithm (24) at discrete time steps of 4 fs. Electrostatic and short-range non-bonded interactions were considered. The particle-mesh Ewald method (25, 26) was used to compute the electrostatic interactions, while a Lennard Jones potential modeled the short-range interactions (only considered within a cut-off of 10 Å). The system was simulated under constant temperature and pressure (NPT) conditions. The temperature was maintained constant at 300 K and pressure to 1 bar, by coupling the system to a velocity-rescaling thermostat (27, 28) (coupling constant $\tau = 0.5$ ps) together with a Parrinello-Rahman barostat (29) (coupling constant $\tau = 5.0$ ps).

2 GPIbα binding site accessible surface (GPIbα-BS-AS)

The GPIbα binding site was constituted by the residues in the A1 domain which were found at a distance smaller than 6 Å from the GPIbα protein, in the X-ray structure of the VWF A1-GPIbα complex (2) (PDB code 1SQ0). The joined surface of the A1 and A2 domains of the VWF (either in contact or separated) was obtained by rolling a sphere with a radius of 5.0 Å on the protein-surface atoms, as described by the Connolly algorithm (30). From that surface, the part corresponding to the GPIbα binding site (in the A1 domain) exposed to the surface was selected, and its area was the GPIbα-BS-AS.

3 Principal component analysis

Principal component analysis (PCA) (31), consisting in the calculation and diagonalization of the covariance matrix of the atomic coordinates, was employed to monitor the inter-domain orientations. The backbone atoms of the β3 strands (of both domains) and the β6 strand of the A2 domain were considered for the PCA calculation. The structures were fitted by superimposing the A1 domain to its initial structure. The structures predicted by molecular docking with Patchdock and Firedock (section 4) were used to generate the diagonalized covariance matrix. Two major PCA eigenvectors constituted 68 % of the possible orientational motions of the A2 domain around the A1 domain. MD trajectories were projected on the 2-dimensional space constituted by these two PCA vectors, to reflect the different orientations adopted by the A2 domain with respect to the A1 domain during the simulations.

4 Molecular docking

Molecular docking was used to generate conformations of the A1 and A2 domains forming a complex. The X-ray structures of the A1 domain (PDB id 1AUQ) (3)) and the A2 domain (PDB id 3GXB) (4) were docked using Patchdock (11). Blind docking, without any constraints, was performed, thus implying no prior bias towards particular conformations. Redundant poses with an

RMSD smaller than 6 Å were clustered yielding an initial set of 11020 possible conformations. They were sorted according to their inter-domain shape complementarity, and 606 conformations were selected for further refinement: the 300 with highest shape complementarity and other 306, selecting one conformation every 35 in the sorted set. Refinement was carried out using Firedock (12). For the resulting conformations, the amount of blockage was quantified by computing the GPIbα binding site accessible surface (GPIbα-BS-AS) on the A1 domain. This quantity was plotted as a function of the Firedock ranking score (an empirical estimate of the binding free energy), and the conformations presenting both substantial blockage and high Firedock scores (more negative values) were considered for further calculations (Fig. S3A). In practice, the ones among the 20 % with lowest GPIbα-BS-AS values and also among the 20 % with lowest Firedock scores were selected. The blocking highly-ranked selected conformations were also clustered according to their RMSD (clustering cutoff of 1.0 nm), yielding 11 representative groups (Fig. S3B). From each group the two (or one in the case of only one) conformations with highest Firedock scores were selected as representative of each group (Fig. S3C), and used as the starting positions for the MD refinement simulations of not connected and bound A1 and A2 domains (see Section 1.1).

Putative poses of the complex were also predicted independently using the RosettaDock protein-protein docking method (32). Its framework relies on identification of low-energy conformations of a protein-protein interaction near a given starting configuration by optimizing the rigid-body orientation and side-chain conformations. 25 initial geometries were provided, which differed in the relative orientation of the two domains. RosettaDock generated 1000 independent structures, and the coordinates for the best model (per starting conformation) were selected.

Molecular docking predicted highly ranked Firedock poses having effect on the GPIbα accessible surface area as well as poses having little effect (Fig. S3A).This was not surprising, given the limitations of docking to predict the distribution of structures occurring naturally. We tested if there was any gain in considering high-score poses instead of any random pose. To this end, we compared the GPIbα-BS-AS of the 11020 poses of the complex predicted by Patchdock, which covered all possible random orientations of the two domains when they are bound to each other, with the values obtained for the 20 % best ranked Firedock poses (Fig. S5). The GPIbα-BS-AS for the Patchdock set did not show any preference for either the blocked (low GPIbα-BS-AS) or the non-blocked (high GPIbα-BS-AS) state. In contrast, by selecting only the poses with high Firedock score (which have high shape complementary and favourable protein-protein interactions between the two domains), there is an increment in the number of structures presenting blockage compared to that number in the Patchdock, the random, set, almost three fold for poses with GPIbα-BS-AS$<$22 nm^2 (compare black with red in Fig. S5 for low GPIbα-BS-AS). This suggest that a structure in the blocked state is favoured over any random structure, due to its high inter-domain shape complementary and favorable protein-protein interactions. This further supports that A2 targets the GPIbα binding site in A1. Furthermore, it justifies our selection criterion, to only structures with both with high blockage and high Firedock score.

5 Cloning, expression and purification of VWF constructs

Plasmid constructs

The cDNAs coding for either the full-length human VWF, the A1 domain (residues 1230 to 1462) and the A2 domain (residues 1494 to 1672), the latter two with 6x His-tag, were cloned into the mammalian expression vector pcDNA3 (33). ΔA1-VWF and ΔA2-VWF mutants were obtained by deleting either the A1 domain (residues 1260 to 1479) or the A2 domain (residues 1493 to 1673) from the full-length cDNA, by site-directed mutagenesis employing the QuickChange kit (Stratagene). All primers are available upon request. The plasmids were sequenced and used to transform Top10 supercompetent cells (Invitrogen). Plasmid purification was performed using the Endofree Plasmid Maxi Kit (QIAGEN).

Cell culture and expression of VWF constructs in HEK293 EBNA cells

HEK293 EBNA cells were cultured in Dulbecco Modified Eagle Medium (DMEM, Invitrogen) with 10 % [v/v] fetal bovine serum (Invitrogen) and 1 % penicillin/streptomycin at 37 °C and 5 % CO_2. HEK293 EBNA cells were transfected with the VWF vectors using Lipofectamine 2000 (Invitrogen) according to the manufacturer's instructions, and a stable cell-line was selected with G418. The recombinant expression of VWF variants was performed in OPTIPRO-SFM (Invitrogen) for 72 hours.

Protein purification

The His-tagged VWF domain constructs were purified employing the His-Pur Ni-NTA Resin (Thermo Scientific) according to the manufacturers instruction for purification of His-tagged proteins using a gravity-flow column.

Multimer analysis

Multimer analysis was performed as previously described (34–36). In brief, VWF multimers of recombinant VWF samples were separated by SDS-agarose electrophoresis, transferred onto a nitrocellulose membrane and detected with anti-human VWF antibody-HRP linked (DAKO) and visualised by luminescence.

6 Atomic force microscopy (AFM)

Chemicals

All chemicals were used in the highest available purity. 3-Aminopropyltriethoxy silane (APTES; SigmaAldrich, Vienna, Austria) was distilled at low pressure and stored under argon in sealed crimp vials over silica gel (to avoid polymerization) at a temperature of -20 °C. MilliQ (Millipore, USA) purified water was used for all aqueous solutions. Triethylamine (TEA, SigmaAldrich, Vienna,

Austria) was stored under argon in the dark to avoid amine oxidation. Chloroform was purchased from J.T. Baker (Griesheim, Germany), argon and N_2 from Linde Gas GmbH (Stadl-Paura, Austria). The heterobifunctional crosslinker maleimide-PEG-NHS was provided by Hermann Gruber, Johannes Kepler University (Linz, Austria) and used as described in (37). Ethylenediaminetetraacetic acid (EDTA) was purchased from VWR International (Vienna, Austria), Hepes and $NiCl_2$ from Merk (Darmstadt Germany), and tris(2-carboxyethyl)phosphine (TCEP) hydrochloride from Molecular Probes, Invitrogen (Vienna, Austria). Disulfide-tris-NTA was generously provided by Prof. Robert Tampé, Biocenter of the Goethe University (Frankfurt am Main, Germany). Mica sheets were bought from Christine Groepl, Electron Microscopy (Tulln, Austria).

AFM cantilevers

For single molecule force spectroscopy (SMFS) experiments non-conductive silicon nitride MSCT tips (Brucker Corporation, USA, D-cantilever, with a $30\,\mathrm{pNnm^{-1}}$ nominal spring constant) were used. The actual spring constant was determined according to Hutter *et al.* (38) using the thermal noise method.

Buffers

The used buffers were TBS buffer (50 mM Tris, and 150 mM NaCl at pH 7.5 adjusted with NaOH), and the Hepes buffer (1 M Hepes at pH 7.5 or pH 9.6, respectively adjusted with NaOH).

Tip and sample chemistry

Amino-functionalization: Commercial MSCT cantilevers were washed with chloroform (3×5 min incubation) and dried in a gentle nitrogen gas stream prior further treatment. For surface functionalization mica sheets were cleaved immediately before further use. The APTES functionalization was performed as described previously (39): A desiccator (5 l) was flooded with argon gas to remove air and moisture. Then two small plastic trays (e.g. the lids of Eppendorf reaction vials) were placed inside the desiccator, 30 ml of APTES and 10ml of triethylamine were separately pipetted into two trays. The AFM tips and the mica sheets were placed nearby on a clean inert surface (e.g. Teflon) and the desiccator was closed. After 120 min of incubation, APTES and triethylamine were removed, the desiccator was again flooded with argon gas for 5 min, and the tips were left inside for two days in order to cure the APTES coating.

Coupling of maleimide-PEG-NHS: The linker coupling was performed as described (37): In brief, APTES functionalized AFM tips or APTES coated mica sheets (samples) were incubated in 0.5 ml (tips) and in 1.5 ml (mica sheets) of a 1 mg/ml solution of maleimide-PEG-NHS in chloroform containing 0.5 % (v/v) of TEA as catalyst for two hours. Subsequently, the tips and mica sheets were rinsed in chloroform (3×5 min) and dried in a gentle stream of nitrogen gas.

Coupling of His6-tagged VWF A1 or A2 domains: The cantilevers and mica sheets were placed on Parafilm in a polystyrene Petri dish and a mixture of 100 μl disulfide-tris-NTA (1 mM in MilliQ

water), 2 μl EDTA (100 mM, pH 7.5 in MilliQ water), 5 μl Hepes (1 M, pH 7.5 in MilliQ water), 2.5 μl TCEP hydrochloride (100 mM in MilliQ water), 2.5 μl Hepes (1 M, pH 9.6 in MilliQ water) was pipetted onto the tips and mica sheets and incubated for two hours. Subsequently tips and mica sheets were washed in TBS buffer (3x5 min) before they were placed on Parafilm in a polystyrene Petri dish and pre-loaded with 50 μl TBS buffer containing 2 μl of 5 mM $NiCl_2$ to obtain a final concentration of 200 μM $NiCl_2$ (pH 7.5) for 5 minutes. Subsequently 100 μl of the His6-tagged protein were mixed with 4 μl of $NiCl_2$ (5 mM) and again incubated for 2 hours. Finally tips and mica sheets were washed 3 times for 5 minutes in TBS and stored in TBS at a temperature of 4 °C until further use.

Single Molecule Force Spectroscopy

SMFS measurements were performed on a scanning probe microscope (Pico SPM Plus setup, Agilent, USA) under near physiological conditions. VWF A1 domains were C-terminally coupled to the AFM tip and VWF A2 domains were C-terminally immobilized to the mica sheet surface. Force distance cycles (FDC) were acquired at room temperature in TBS buffer by approaching the AFM tip towards the surface, followed by its retraction. Specific interactions were discerned from nonspecific adhesion by a differing approach and retraction force signal. To have an unbiased choice of binding events, FDC displaying a characteristic worm-like-chain-type force signal, as well as FDC not showing such behavior, were included for further analysis. To prove the specificity of the interactions between the A1 and the A2 domain, control experiments were carried out either in the presence of 0.1 mg/ml soluble A2 domains or by replacing either the A1 or the A2 domain by VWF A3 domain. The position of the tip relative to the surface was changed every 200 FDC, to statistically avoid position dependent artifacts. Four tips (each functionalized either with the VWF A1 domain or the VWF A3 domain) were utilized. At least 1000 FDC were recorded for each of the tips at a pulling speed of 600 nm/s. The number of binding events in relation to the whole number of acquired FDC was computed. It should be noted that unbinding events occur sequentially, as it is very unlikely to have identical elongations for two unbinding events simultaneously (40). In fact, multiple binding events were observed only in rare cases (at the most two bindings and in less than 4%), and they were not considered for further analysis. The elongation L of the pulled construct (A1, A2, coating molecules, and linkers) was monitored during the experiments. Its expectaction value (EV) was computed from his probability distribution as $EV = \sum_i P_i Li$, where P_i is the probability of occurrence of an elongation L_i.

7 Microfluidic experiments

For distinct shear rate application, air-pressure driven microfluidic channels (BioFlux, USA) were coated with 50 μg/mL recombinant wild-type VWF over night at 37 °C. For preparation of the perfusion media, blood was collected from healthy volunteers using sodium citrated blood vacuum collection tubes. The study was conducted in conformity to the Declaration of Helsinki (41) and

to The International Conference on Harmonization of Technical Requirements for Registration of Pharmaceuticals for Human Use (ICH) Guidelines, available at http://www.ich.org, accessed in October 2010. It was approved by the Ethics Committee of the Medical Faculty Mannheim, Heidelberg University (Mannheim, Germany). Appropriate informed consent was obtained from all subjects. To functionally characterize the impact of the VWF A2 domain on the GPIbα-VWF A1 domain interaction, wild-type VWF coated microfluidic channels were mounted onto an inverted fluorescence microscope (Zeiss Axio Observer Z.1, Zeiss AG, Oberkochen, Germany) and perfused as previously published (42), with the wild-type VWF, VWF with the A2 domain deleted, or VWF with the A1 domain deleted. Briefly, washed platelets were used in a concentration of 200000 per μl stained with Celltrace calcein-green (Invitrogen, USA). This solution was supplemented with 45 % washed haematocrit in HEPES buffered ringer solution. Focusing on the shear dependent ability to form platelet binding strings, the plasmatic VWF fraction was replaced with 10 μg/mL recombinant VWF, either wild-type or with the A1 or the A2 domain deleted. Live cell fluorescence videos were taken at two frames per second at various shear rates in the range of $500\,\mathrm{s}^{-1}$ to $4000\,\mathrm{s}^{-1}$ (with a nominal shear rate precision of $36\,\mathrm{s}^{-1}$). For image analysis we used the ZEN package (Zeiss AG, Jena, Germany) and the open-source software ImageJ (V. 1.46r, National Institute of Health, USA).

Supporting material references

[1] Zhou, Y.-F., E. T. Eng, N. Nishida, C. Lu, T. Walz, and T. A. Springer, 2011. A pH-regulated dimeric bouquet in the structure of von Willebrand factor. *EMBO J* 30:4098–4111.

[2] Dumas, J. J., R. Kumar, T. McDonagh, F. Sullivan, M. L. Stahl, W. S. Somers, and L. Mosyak, 2004. Crystal structure of the wild-type von Willebrand factor A1-glycoprotein Ibα complex reveals conformation differences with a complex bearing von Willebrand disease mutations. *J Biol Chem* 279:23327–23334.

[3] Emsley, J., M. Cruz, R. Handin, and R. Liddington, 1998. Crystal structure of the von Willebrand factor A1 domain and implications for the binding of platelet glycoprotein Ib. *J Biol Chem* 273:10396–10401.

[4] Zhang, Q., Y.-F. Zhou, C.-Z. Zhang, X. Zhang, C. Lu, and T. A. Springer, 2009. Structural specializations of A2, a force-sensing domain in the ultralarge vascular protein von Willebrand factor. *Proc Natl Acad Sci USA* 106:9226–9231.

[5] Matsui, T., K. Titani, and T. Mizuochi, 1992. Structures of the asparagine-linked oligosaccharide chains of human von Willebrand factor. Occurrence of blood group A, B, and H(O) structures. *J Biol Chem* 267:8723–8731.

[6] Woods Group, 2005-2013. GLYCAM web. *In: Woods RJ, editor. Athens, GA: Complex Carbohydrate Research Center, The University of Georgia.* .

[7] Schrödinger, LLC, 2010. The PyMOL molecular graphics system, version 1.3r1.

[8] Van der Spoel, D., E. Lindahl, B. Hess, G. Groenhof, A. E. Mark, and H. J. C. Berendsen, 2005. GROMACS: fast, flexible, and free. *J Comput Chem* 26:1701–1718.

[9] Hess, B., C. Kutzner, D. van der Spoel, and E. Lindahl, 2008. GROMACS 4: Algorithms for highly efficient, load-balanced, and scalable molecular simulation. *J Chem Theory Comput* 4:435–447.

[10] Pronk, S., S. Pll, R. Schulz, P. Larsson, P. Bjelkmar, R. Apostolov, M. R. Shirts, J. C. Smith, P. M. Kasson, D. van der Spoel, B. Hess, and E. Lindahl, 2013. GROMACS 4.5: a high-throughput and highly parallel open source molecular simulation toolkit. *Bioinformatics* 29:845–854.

[11] Schneidman-Duhovny, D., Y. Inbar, R. Nussinov, and H. J. Wolfson, 2005. Patchdock and Symmdock: servers for rigid and symmetric docking. *Nucleic Acids Res* 33:W363–W367.

[12] Mashiach, E., D. Schneidman-Duhovny, N. Andrusier, R. Nussinov, and H. J. Wolfson, 2008. Firedock: a web server for fast interaction refinement in molecular docking. *Nucleic Acids Res* 36:W229–W232.

[13] Canis, K., T. A. J. McKinnon, A. Nowak, M. Panico, H. R. Morris, M. Laffan, and A. Dell, 2010. The plasma von Willebrand factor O-glycome comprises a surprising variety of structures including abh antigens and disialosyl motifs. *J Thromb Haemost* 8:137–145.

[14] D. van der Spoel, B. H., E. Lindahl, and *et al.*, 2010. Gromacs User Manual version 4.5.6. www.gromacs.org.

[15] Hornak, V., R. Abel, A. Okur, B. Strockbine, A. Roitberg, and C. Simmerling, 2006. Comparison of multiple amber force fields and development of improved protein backbone parameters. *Proteins: Struct Funct Bioinf* 65:712–725.

[16] Best, R. B., and G. Hummer, 2009. Optimized molecular dynamics force fields applied to the helix-coil transition of polypeptides. *J Chem Phys B* 113:9004–9015.

[17] Lindorff-Larsen, K., S. Piana, K. Palmo, P. Maragakis, J. L. Klepeis, R. O. Dror, and D. E. Shaw, 2010. Improved side-chain torsion potentials for the Amber ff99SB protein force field. *Proteins: Struct Funct Bioinf* 78:1950–1958.

[18] Kirschner, K. N., A. B. Yongye, S. M. Tschampel, J. Gonzlez-Outeirio, C. R. Daniels, B. L. Foley, and R. J. Woods, 2008. GLYCAM06: a generalizable biomolecular force field. Carbohydrates. *J Comput Chem* 29:622–655.

[19] Jorgensen, W. L., J. Chandrasekhar, J. D. Madura, R. W. Impey, and M. L. Klein, 1983. Comparison of simple potential functions for simulating liquid water. *J Chem Phys* 79:926–935.

[20] Joung, I. S., and T. E. Cheatham, 2008. Determination of alkali and halide monovalent ion parameters for use in explicitly solvated biomolecular simulations. *J Chem Phys B* 112:9020–9041.

[21] Hess, B., H. Bekker, H. J. C. Berendsen, and J. G. E. M. Fraaije, 1997. LINCS: A linear constraint solver for molecular simulations. *J Comput Chem* 18:1463–1472.

[22] Feenstra, K. A., B. Hess, and H. J. C. Berendsen, 1999. Improving efficiency of large time-scale molecular dynamics simulations of hydrogen-rich systems. *J Comput Chem* 20:786–798.

[23] Miyamoto, S., and P. A. Kollman, 1992. Settle: An analytical version of the SHAKE and RATTLE algorithm for rigid water models. *J Comput Chem* 13:952–962.

[24] Hockney, R. W., and J. W. Eastwood, 1988. Computer simulation using particles. Bristol: Hilger.

[25] Darden, T., D. York, and L. Pedersen, 1993. Particle mesh Ewald: An Nlog(N) method for Ewald sums in large systems. *J Chem Phys* 98:10089–10092.

[26] Essmann, U., L. Perera, M. L. Berkowitz, T. Darden, H. Lee, and L. G. Pedersen, 1995. A smooth particle mesh Ewald method. *J Chem Phys* 103:8577–8593.

[27] Bussi, G., D. Donadio, and M. Parrinello, 2007. Canonical sampling through velocity rescaling. *J Chem Phys* 126:014101 – 014101–7.

[28] Berendsen, H. J. C., J. P. M. Postma, W. F. van Gunsteren, A. DiNola, and J. R. Haak, 1984. Molecular dynamics with coupling to an external bath. *J Chem Phys* 81:3684–3690.

[29] Parrinello, M., and A. Rahman, 1981. Polymorphic transitions in single crystals: A new molecular dynamics method. *J Appl Phys* 52:7182–7190.

[30] Connolly, M. L., 1983. Analytical molecular surface calculation. *J Appl. Crystallogr.* 16:548–558.

[31] Amadei, A., A. B. M. Linssen, and H. J. C. Berendsen, 1993. Essential dynamics of proteins. *Proteins: Struct., Funct., Gen.* 17:412–425.

[32] Lyskov, S., and J. J. Gray, 2008. The RosettaDock server for local protein-protein docking. *Nucleic Acids Res* 36:W233–W238.

[33] Schneppenheim, R., J. J. Michiels, T. Obser, F. Oyen, A. Pieconka, S. Schneppenheim, K. Will, B. Zieger, and U. Budde, 2010. A cluster of mutations in the D3 domain of von Willebrand factor correlates with a distinct subgroup of von Willebrand disease: type 2A/IIE. *Blood* 115:4894–4901.

[34] Budde, U., R. Schneppenheim, J. Eikenboom, A. Goodeve, K. Will, E. Drewke, G. Castaman, F. Rodeghiero, A. B. Federici, J. Batlle, A. Prez, D. Meyer, C. Mazurier, J. Goudemand, J. Ingerslev, D. Habart, Z. Vorlova, L. Holmberg, S. Lethagen, J. Pasi, F. Hill, and I. Peake, 2008. Detailed von Willebrand factor multimer analysis in patients with von willebrand disease in the european study, molecular and clinical markers for the diagnosis and management of type 1 von willebrand disease (MCMDM-1VWD). *J Thromb Haemost* 6:762–771.

[35] Budde, U., R. Schneppenheim, H. Plendl, J. Dent, Z. M. Ruggeri, and T. S. Zimmerman, 1990. Luminographic detection of von Willebrand factor multimers in agarose gels and on nitrocellulose membranes. *Thromb Haemost* 63:312–315.

[36] Schneppenheim, R., H. Plendl, and U. Budde, 1988. Luminography–an alternative assay for detection of von Willebrand factor multimers. *Thromb Haemost* 60:133–136.

[37] Crosslinkers and protocols for AFM Tip functionalization. Johannes Kepler University, Linz, Austria. March-October 2013. Web. 08 April 2015. http://www.jku.at/biophysics/content/e257042 .

[38] Hutter, J. L., and J. Bechhoefer, 1993. Calibration of atomic-force microscope tips. *Rev Sci Instrum* 64:1868–1873.

[39] Ebner, A., P. Hinterdorfer, and H. J. Gruber, 2007. Comparison of different aminofunctionalization strategies for attachment of single antibodies to AFM cantilevers. *Ultramicroscopy* 107:922–927.

[40] Zhu, R., S. Howorka, J. Prll, F. Kienberger, J. Preiner, J. Hesse, A. Ebner, V. P. Pastushenko, H. J. Gruber, and P. Hinterdorfer, 2010. Nanomechanical recognition measurements of individual dna molecules reveal epigenetic methylation patterns. *Nat Nanotechnol* 5:788–791.

[41] RICKHAM, P. P., 1964. Human Experimentation: Code of Ethics of World Medical Association. DECLARATION OF HELSINKI. *Br Med J* 2:177.

[42] Brehm, M. A., V. Huck, C. Aponte-Santamaría, T. Obser, S. Grässle, F. Oyen, U. Budde, S. Schneppenheim, C. Baldauf, F. Gräter, S. W. Schneider, and R. Schneppenheim, 2014. Von Willebrand disease type 2A phenotypes IIC, IID and IIE: A day in the life of shear-stressed mutant von Willebrand factor. *Thromb Haemost* 112:96–108.